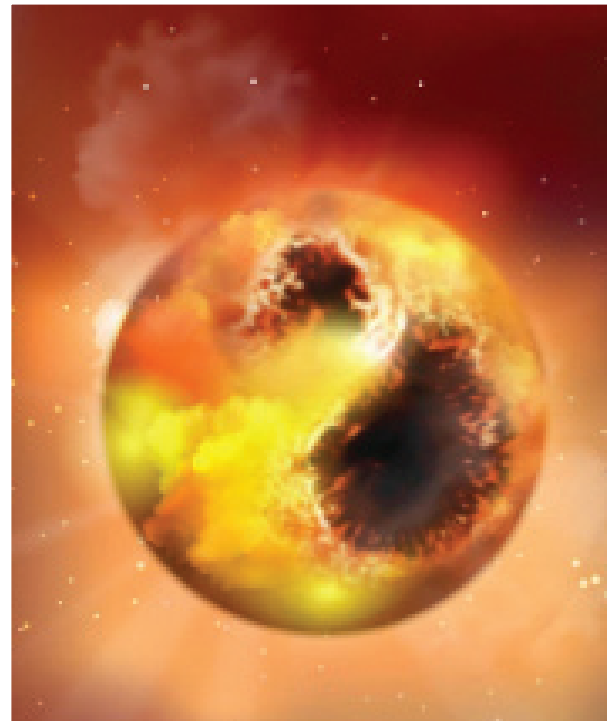
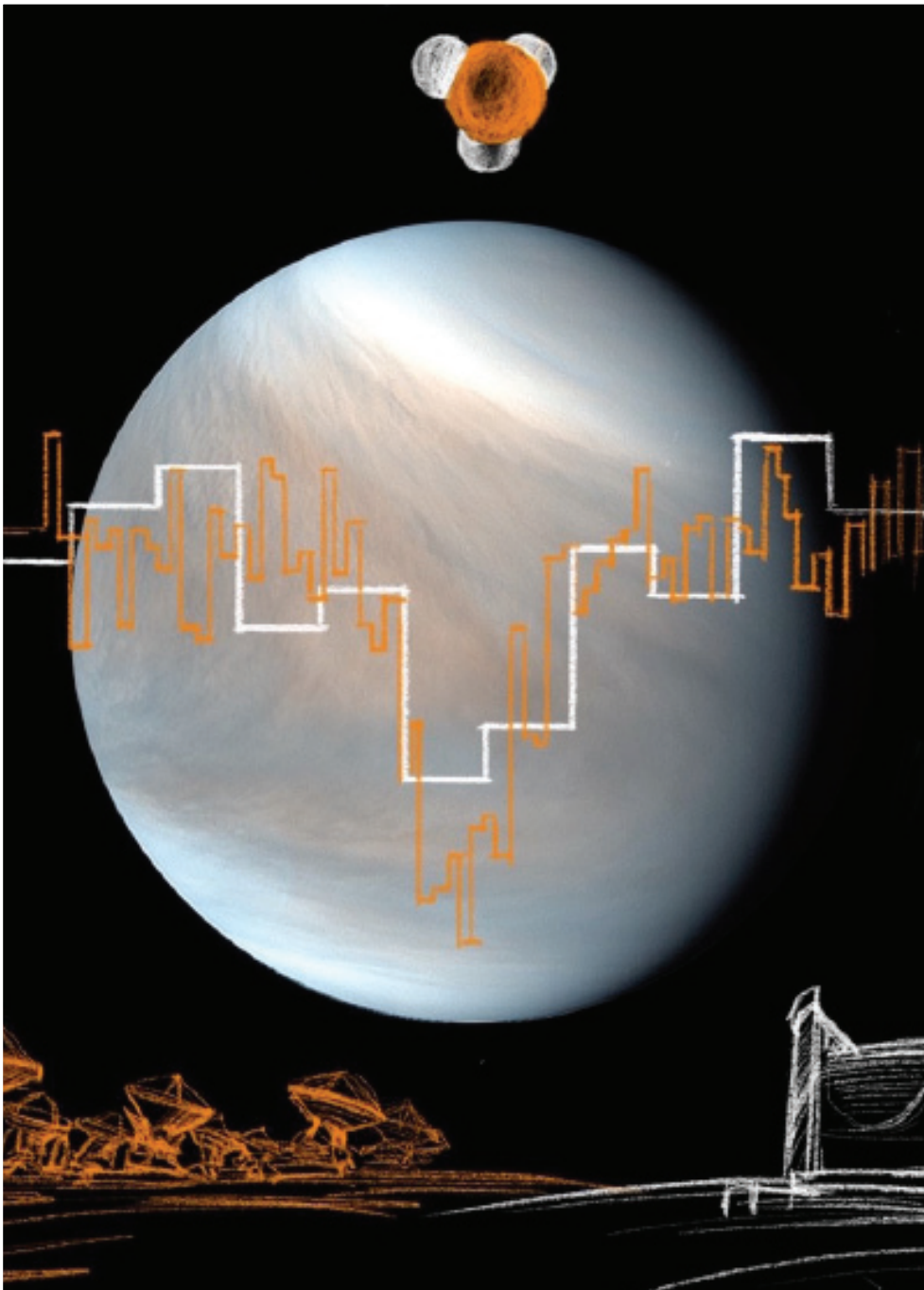


East Asian Observatory News



East Asian Observatory News

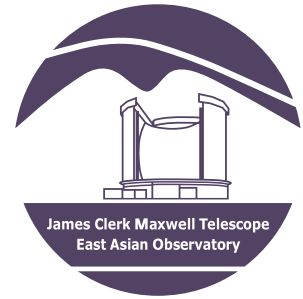
Issue #6, December 2020

In this Issue:

Director's Corner - P. Ho	3
JCMT Discovers Phosphine in the Clouds of Venus - J. Greaves, et al.	4
Using CO Line Ratios to Trace Compressed Areas in Bubble N131 - C. Zhang	7
Interplay Between Magnetic Fields, Gravity, Turbulence, and Stellar Feedback in Sh2-201 Revealed by SCUBA-2 and POL-2 - E. Chakali	9
First Sub-pc Scale Mapping of Magnetic Fields in the Vicinity of a Very Low Luminosity Object, L1521F-IRS - A. Soam	12
Betelgeuse Was Not Fainter Because of Dust - T. Dharmawardena, et. al	14
Two Sub-Millimetre Bright Protoclusters Bounding the Epoch of Peak Star-Formation Activity - K. Lacaille	17
Dense Molecular Gas and Star Formation in Nearby Galaxies - Recent Results from MALATANG - X. Jiang	19
JCMT SCOPE Survey Reveals "Treasure Map" for Star Formation - T. Liu, et. al	21
A Decade in the Making: Celebrating a Year of Successful Remote Observing - H. Parsons	23
'Ū'ū Commissioning Update - D. Bintley	26
JCMT Ice and Snow Melting Program - C. Walther	27
Maunakea Wonders Teacher Workshop - C. Matulonis	28
A Hui Hou - J. Hoge	30
2020 - The EAO 'Ohana's Year in Review - C. Matulonis	30

This copy of the East Asian Observatory News was produced and edited by Callie Matulonis, Steve Mairs, and Harriet Parsons with additional editorial assistance from Maren Purves.

If you wish to submit an article for the next EAO Newsletter please send an e-mail to: newsletter@eaobservatory.org



East Asian Observatory
660 North A'Ohōkū Place
Hilo, Hawai'i, 96720
USA

www.eaobservatory.org

helpdesk@eaobservatory.org



weChat:
EAO-JCMT



From the front cover.

Left: JCMT Discovers Phosphine in the Clouds of Venus (Story on Page 4) Image Credit: Joanna Pełkowska, PhD

Top Right: An artist's impression of the Red Supergiant Betelgeuse. Betelgeuse Was Not Fainter Because of Dust (Story on Page 14) Image Credit: Graphics Department/ MPIA.

Bottom Right: EAO Chief Engineer Craig Walther performing maintenance on Nāmakanui. ('Ū'ū Commissioning Update on Page 26)

From the back cover: The conjunction of Jupiter and Saturn as observed by SCUBA-2 at 850 microns on December 21st, 2020.

Director's Corner

Paul Ho, Director General of EAO

In 2020, the EAO continues in her 6th year of operating the JCMT. It has been a momentous and difficult year not only for the JCMT, but also for the entire world because of the coronavirus pandemic.

On March 18, 2020, JCMT operations were halted and the staff were asked to work from home, as COVID-19 cases began to ramp up in the United States. All of the Maunakea Observatories had stopped operations as part of the "Stay at home" Proclamation by Hawaii Governor Ige. The EAO implemented a strict policy of social distancing, wearing of masks, sanitizing of work environments, and restricted access to the observatory. As Hawai'i restricted incoming flights and imposed quarantine on off-island visitors, the COVID-19 cases subsided enough after two months that the Maunakea Observatories were allowed to return to operations.

The JCMT resumed science operations on May 14, 2020. Since then, Hawai'i has suffered a second wave

of COVID-19 that peaked in August 2020. The JCMT has continued to operate, given that we are in full remote operations mode. On-site maintenance has been reduced to typically two times a week, with a minimal crew. Staff are continuing to work from home, with very minimal presence in our offices. We stop whenever any staff reports being unwell, and the building is cleaned thoroughly before reopening, while contact tracing is immediately followed up. With the full cooperation of the EAO staff, the JCMT has remained in a safe state so far.

All of our instruments: SCUBA-2, HARP, and Nāmakānuī, are working smoothly. Our fault rate has remained at about 3-5%. Even with the lost time due to COVID-19, the Large Programs have made good progress: all seven 16A programs are essentially completed, four out of five 17B programs are mostly completed, and 20A programs are underway.

On the financial front, the EAO con-

tinues to suffer from the reduced funding from Japan. With the help of all the other JCMT funding partners, as well as an SBAPPP loan from the US CARES COVID-19 stimulus initiative, the EAO was able to complete operations during this very difficult year.

In terms of expanding the EAO partnership, we have been limited in our abilities to work directly with the new communities. In December 2020, a JCMT users workshop was held online, with participants from Malaysia, Thailand, Indonesia, and Vietnam. We look forward to working with these regions who are on observer status, and also India, during 2021, in order to welcome them into our EAO family as partners.¹

We wish that our EAO family, our users community and their family and friends, will all keep safe and healthy during these uncertain times.

¹ See www.eaobservatory.org/jcmt/proposals/eao_eligibility/ for more information on EAO Eligibility and Funding Partners.

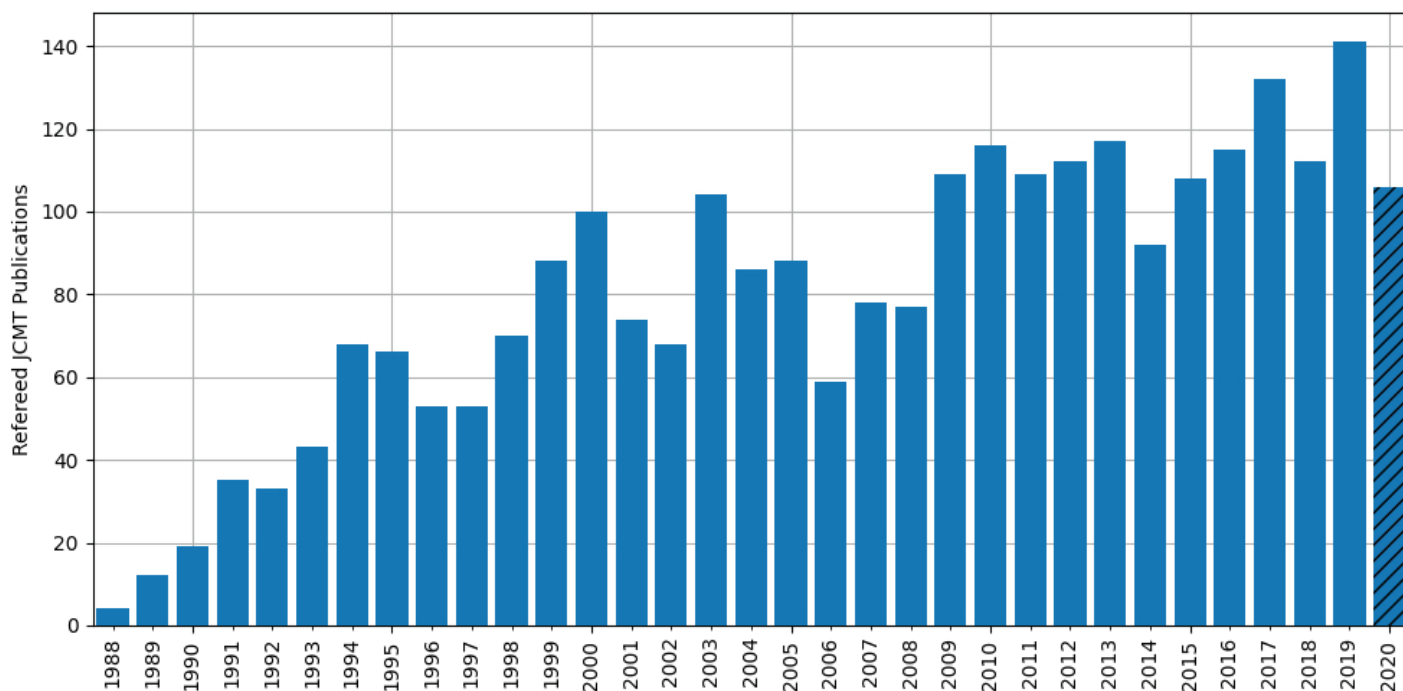


Figure 1: JCMT refereed publications through October 2020. Shading indicates that 2020 is not yet complete. Visit <https://www.eaobservatory.org/jcmt/science/publications/> for more information.

JCMT Discovers Phosphine in the Clouds of Venus

Jane Greaves, Cardiff University, UK and Steve Mairs, Senior Scientist, EAO/JCMT

In September, 2020, an international team of astronomers, led by Professor Jane Greaves of Cardiff University, UK (see Figure 2), announced the discovery of phosphine (PH_3) in the clouds of Venus [Greaves et al., 2020a]. The announcement was broadcast on media outlets all over the world, fuelled by excitement of the molecule's potential role as a biomarker. On Earth, phosphine gas is only made industrially, or by microbes that thrive in oxygen-free environments.

The first detection of phosphine in the clouds of Venus was made using the JCMT (see Figure 3). The observations were carried out over 5 mornings in June 2017, targeting the PH_3 (1-0) line at a rest frequency of 266.9447 GHz with the (now retired) instrument, RxA3m. Backlit by the warmer clouds lower in the

atmosphere, phosphine reveals itself as a faint absorption line as PH_3 molecules in the high altitude cloud decks leave their fingerprints on the incoming light. With the success of the JCMT observations, the team was then awarded time to follow up their discovery with 45 telescopes of the Atacama Large Millimeter/submillimeter Array (ALMA) in March 2019 where a strong phosphine absorption line appeared to confirm the result.

Shortly after the paper was published, an invigorated astrobiology and planetary science community debated the signal. In this process of closely examining the data, Villanueva et al. discovered an issue with ALMA's bandpass calibration. The effect was a spurious ripple in the spectrum that had an impact on the strength of the phosphine

detection. ALMA staff addressed the issue and released the newly-calibrated and reprocessed interferometric data to the public archive on November 17th, 2020.

Greaves and her team reanalyzed the ALMA data after the calibration correction and noted that the PH_3 absorption line was still recovered at $\sim 5\sigma$ confidence [Greaves et al., 2020b] (see Figure 4). The newly processed ALMA data yields a localized abundance of phosphine peaking at ~ 5 parts-per-billion (ppb) with spatial variations. The planet-averaged PH_3 abundance was found to be $\sim 1-4$ ppb, which is $\sim 2-5$ times lower than the original ALMA data suggested. By contrast, the JCMT spectrum gives evidence of atmospheric phosphine abundances of ~ 20 ppb. It is possible that there is an order of magnitude tem-



Figure 2: The 19 authors who contributed to the first detection of phosphine on Venus. From right to left Top row: Jane Greaves, Helen Fraser, Annabel Cartwright, Clara Sousa-Silva, Sara Seager, Middle top row: Hideo Segawa, Emily Drabek-Maunder, Janusz Petkowski, Paul Rimmer. Middle bottom row: Zhuchang Zhan, William Bains, Ingo Mueller-Wodarg, Sukrit Ranjan. Bottom row: Per Friberg, Anita Richards, Jim Hoge, E'Lisa Lee, Iain Coulson, David Clements. Artwork credit: Joanna Pełtkowska, PhD.

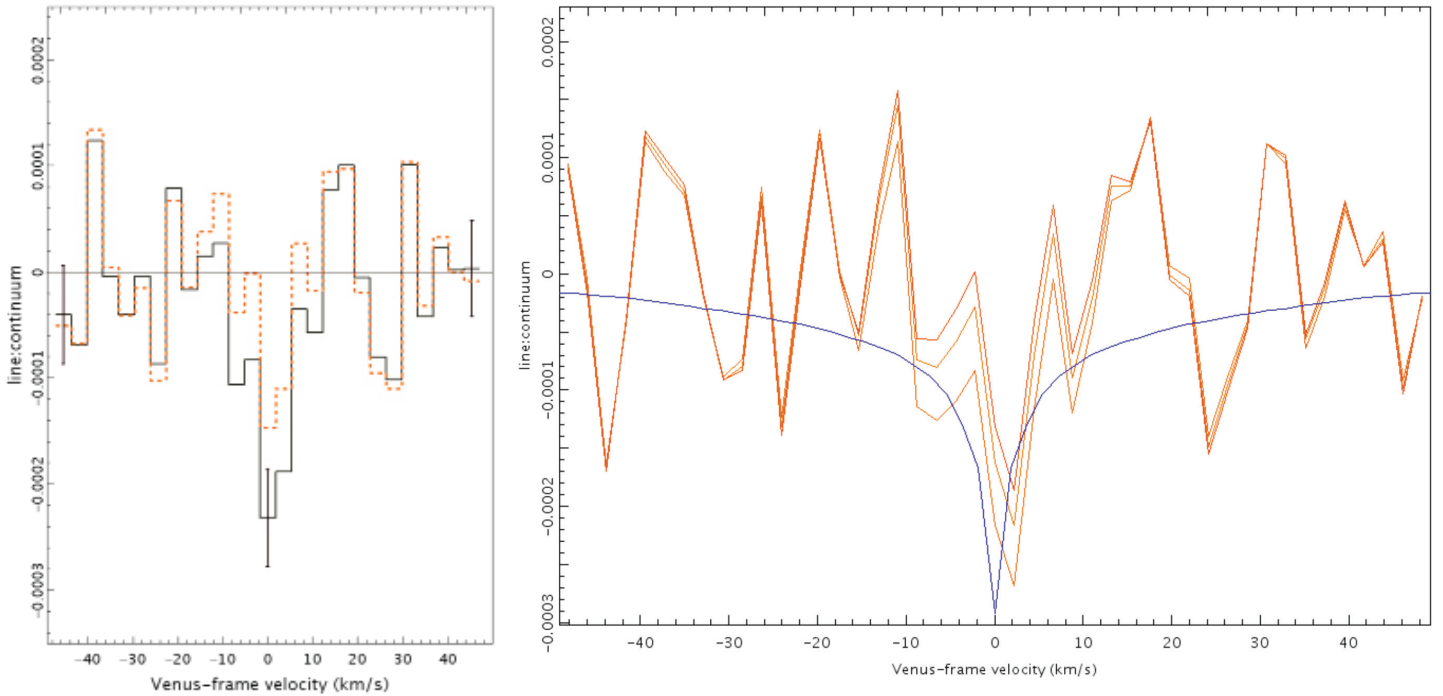


Figure 3: Taken from Greaves et al., 2020a and Greaves et al., 2020b. Left Panel: Spectrum of PH_3 1-0 in Venus' atmosphere as observed with the JCMT. The histograms show the least and most conservative solutions after fitting and removing spectral ripple (see Supplementary Materials), with the residual line inside velocity-ranges of respectively $|v| = 8$ km/s (solid, black) and $|v| = 2$ km/s (dashed, orange). The data have been binned on the x-axis for clarity; representative 1σ error bars are $0.46 \cdot 10^{-4}$ in line:continuum per 3.5 km/s spectral bin. Right Panel: JCMT spectrum obtained with interpolation regions $\pm(2,5,8)$ km/s (top to bottom curves). A 10 ppb radiative transfer model is overlaid (blue curve), without removing the modelled line wings.

poral variation that takes place on short timescales, as the JCMT and ALMA data were collected 2 years apart. Spatial and temporal variations in gas abundance have been documented in other planets, such as the case of methane spikes on Mars observed by NASA's Curiosity rover. The lifetime of phosphine in the Venusian atmosphere is calculated to be no longer than 10^3 seconds, either because it is destroyed on a shorter timescale (for instance, by collisional interactions low in the atmosphere by free radicals high in the atmosphere) or because it is transported to a region where it is rapidly destroyed. Independent PH_3 measurements suggest a possible altitude dependence where abundances may be under ~ 5 ppb at 60+ km and up to ~ 100 ppb at 50+ km [Greaves et al., 2020b].

With the exciting prospect of the existence of phosphine tentatively confirmed at ALMA, the analysis of the theoretical phosphine abundance based on a series of production mechanisms presented in the original paper remains intriguing.

There are several natural processes on Venus that can produce phosphine including photochemistry, minerals blown upwards from the surface, volcanoes, lightning, and meteoric activity. These natural sources together are expected to produce several orders of magnitude less phosphine than is observed. The authors conclude that "if no known chemical process can explain the presence of PH_3 in the middle/upper atmosphere of Venus, then it must be produced by a process not previously considered plausible for Venusian conditions. This could be unknown photochemistry or geochemistry, or possibly life." [Greaves et al., 2020a].

The idea that high clouds on Venus could offer a home for aerial microbes has existed for over 50 years [Morowitz & Sagan, 1967]. High in the clouds, bacteria would have access to water and sunlight while experiencing temperatures and pressures that are much more likely suited for habitation than the extreme conditions found on the planet's surface. There are, howev-

er, other issues such as the need for potential microbes to tolerate very high levels of acidity as the Venusian clouds are thoroughly peppered with sulphuric acid. One proposed solution to this problem is a mechanism in which potential microbes could shield themselves inside shells of sulfur as a form of protection from the surrounding acid.

Searching for phosphine as a bio-signature gas of non-oxygen-using life on planets around other stars has previously been discussed in the literature specifically because normal chemistry makes so little of the molecule [Sousa-Silva et al., 2020]. This is based on the fact that known anaerobic bacteria on Earth can absorb phosphate minerals, add hydrogen, and ultimately expel phosphine gas. The team that discovered phosphine on Venus found that in order to create the observed quantity, terrestrial organisms would only need to work at $\sim 10\%$ (for 10 ppb) of their maximum productivity. Any microbes on Venus would likely be very different to their Earth cousins.

While the discovery of phosphine is significant, the team readily acknowledges that confirming the presence of “life” needs much further work. The team is now eagerly awaiting more telescope time to establish whether the phosphine is in a relatively temperate part of the clouds, to investigate spatial and temporal variations, and to search for other gases associated with life.

At the time of observations, both ALMA and the JCMT were working at the limit of observatory capabilities. Recently, however, the JCMT instrument used in the Venus study (RxA3m) has been replaced by a new 230 GHz receiver named ‘Ü’ü, a

dual sideband heterodyne camera with the capability to measure linear polarization. Initial results show that it is four times more sensitive than its predecessor, opening a wide range of possibilities for continuing research on Venus using the JCMT. This is just the beginning.

The authors of Greaves et al. 2020a are: Jane S. Greaves (Cardiff University, UK), Anita M. S. Richards (Jodrell Bank Centre for Astrophysics, The University of Manchester, UK), William Bains (MIT, USA), Paul Rimmer (Department of Earth Sciences and Cavendish Astrophysics, University of Cambridge and MRC Laboratory of Molecular Biology, Cambridge, UK), Hideo Sagawa (Kyoto Sangyo

University, Japan), David L. Clements (Imperial College London, UK), Sara Seager (MIT, USA), Janusz J. Petkowski (MIT, USA), Clara Sousa-Silva (MIT), Sukrit Ranjan (MIT), Emily Drabek-Maunder (Cardiff and Royal Observatory Greenwich, UK), Helen J. Fraser (The Open University, UK), Annabel Cartwright (Cardiff University, UK), Ingo Mueller-Wodarg (Imperial College, UK), Zhuchang Zhan (MIT, USA), Per Friberg (EAO/JCMT), Iain Coulson (EAO/JCMT), E’Lisa Lee (EAO/JCMT) and Jim Hoge (EAO/JCMT).

This research is published in Nature Astronomy (Greaves, et al. 2020a) and can be found at www.nature.com/articles/s41550-020-1174-4.

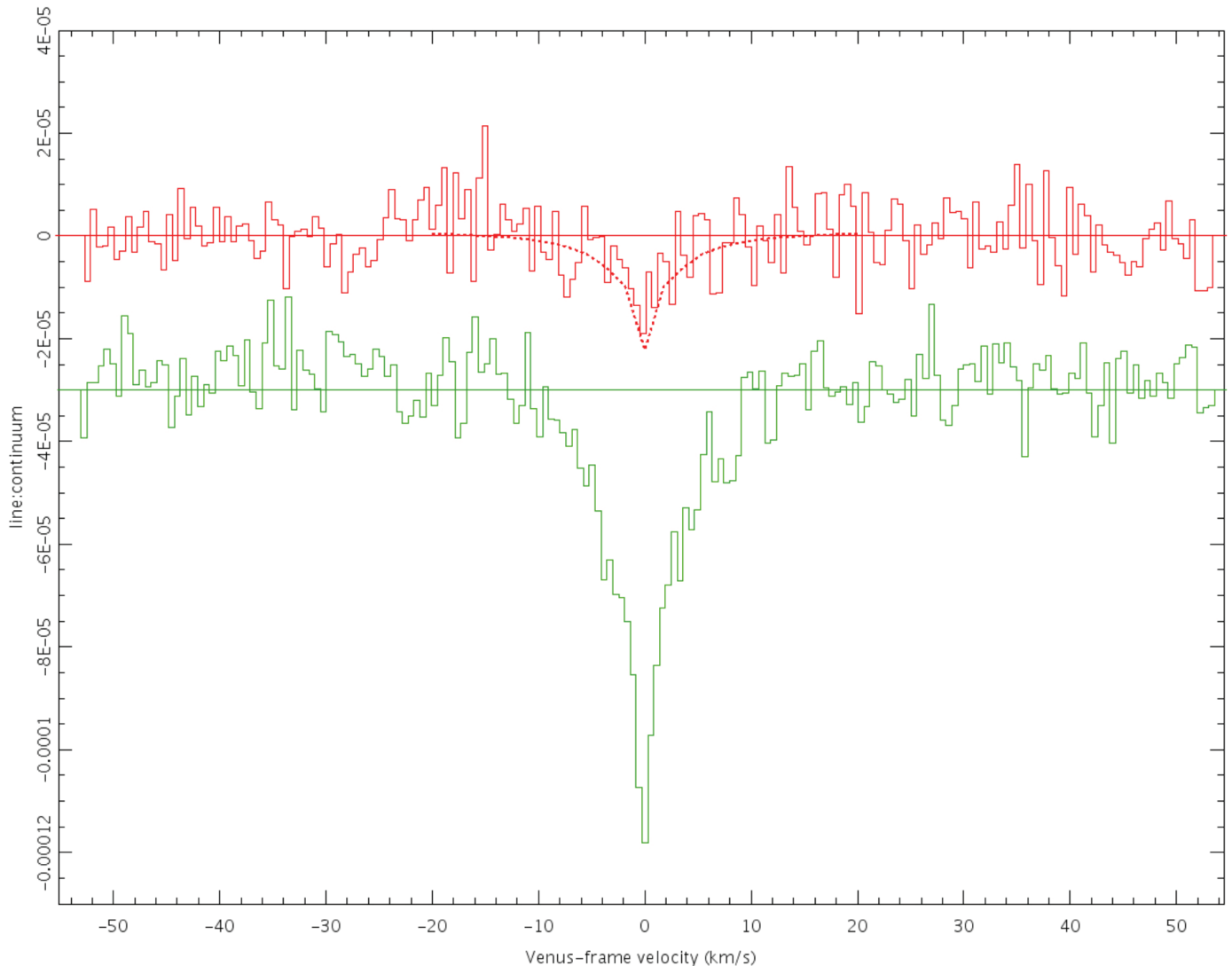


Figure 4. Taken from Greaves et al. 2020b. The line:continuum for PH_3 (red, top) and HDO (green; bottom - offset for clarity). No post-processing has been performed on these spectra, apart from dividing the line products by 13.77 Jy/beam , the estimated continuum signal (considered to be accurate to $\sim 10\%$). Overlaid is our PH_3 radiative transfer model, scaled to 1 ppb. To simulate the effects of a bandpass solution of up to 12th -order, which may remove features more than $\sim 20 \text{ km/s}$ wide, we subtracted a 12th -order polynomial from the original model (interpolating across $\pm 10 \text{ km/s}$; results in $\sim 25\%$ signal-loss at line-minimum).

Using CO line Ratios to Trace Compressed Areas in Bubble N131

Chuan-Peng Zhang, Chinese Academy of Sciences, China and Guang-Xing Li, Yunnan University, China

N131 is a typical infrared dust bubble showing an expanding ring-like shell. In this work (Zhang et al. 2019 A&A, 631:A110), we study the CO line ratios that can be used to trace the interaction between the hot stellar winds and the cold molecular expanding bubble. We carried out CO (3-2) observations toward bubble N131 using the JCMT, and derived line ratios by combining these observations with our previous CO (2-1) and CO (1-0) data from IRAM 30m observations. To trace the interaction between the molecular gas and the ionized gas in the HII region, we used RADEX to model the dependence of the CO line ratios on kinetic temperature and H2 volume density, and examined the abnormal line ratios based on other simulations. We present CO (3-2), CO (2-1), and CO (1-0) integrated intensity maps (see Figure 5).

Bubble N131 has an inner minor radius of 13 pc and an inner major radius of 15 pc at a kinetic distance of ~ 8.6 kpc, and the center coordinates are RA(J2000) = $19^{\text{h}}52^{\text{m}}21.^{\text{s}}5$, Dec(J2000) = $+26^{\circ}21'24.''0$. A ring-like shell is visible at 8.0 and 24 micron and is associated with CO emission (see Figure 5). Two giant elongated molecular clouds are located at opposite sides of the ring-like shell, and together, they exhibit a large velocity gradient. In addition, there is a huge cavity inside the bubble that is visible in the 5.8-500 micron emission. The column density, excitation temperature, and velocity of the CO (1-0) emission show a possibly stratified structure from the inner to outer rims of the ring-like shell. These suggest that bubble N131 has an expanding shell caused by feedback of strong stellar winds from the star formation at the center of the bubble.

The infrared dust bubble N131 originates from expanding HII regions, but the HII region inside has

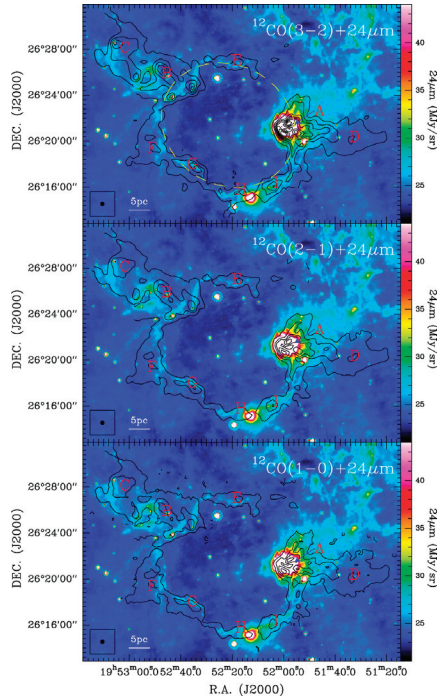


Figure 5: Integrated intensity maps of CO (3-2) (top), CO (2-1) (middle), and CO (1-0) (bottom) lines with a velocity range from -16.0 to -5.0 km/s superimposed on 24 micron emission. The contour levels in each CO map start at 5σ in steps of 10σ . The letters and the ellipse indicate the positions of nine molecular clumps (A - I) and the ring-like shell of the bubble, respectively. The angular resolution ($22.5''$) is indicated in the bottom left corner of each panel.

been extinguished (Zhang et al. 2013, 2016). Figure 6 clearly shows that most parts of the inner rims of the ring-like shell have higher integrated intensity ratios (e.g., $W_{\text{CO}(3-2)}/W_{\text{CO}(2-1)} \geq 0.8$ and $W_{\text{CO}(2-1)}/W_{\text{CO}(1-0)} \geq 1.2$) than the outer rims. Additionally, the most notable discrepancy between the two ratio distributions is that at the inner rims of the ring-like shell near clumps G and H, the ratio $W_{\text{CO}(3-2)}/W_{\text{CO}(2-1)}$ is much higher than in other regions (except for the complicated clump A) but the ratio $W_{\text{CO}(2-1)}/W_{\text{CO}(1-0)}$ is not. Conversely, at the inner rims near clump B, the ratio $W_{\text{CO}(2-1)}/W_{\text{CO}(1-0)}$ is much higher

than in other regions but the ratio $W_{\text{CO}(3-2)}/W_{\text{CO}(2-1)}$ is not. This may suggest that the inner rims of the ring-like shell near clumps G and H have a relatively high kinetic temperature up to the excitation temperature of high transition level of CO (3-2), leading to stronger CO (3-2) emission than in other regions; while the inner rims near clump B have a relatively low kinetic temperature just up to the low transition level of CO (2-1), leading to stronger CO (2-1) emission than in other regions. This also suggests that the inner rims of the ring-like shell were compressed by strong stellar winds from the bubble insides (see also discussion in Nishimura et al. 2015).

To trace the compressed inner rims of the ring-like shell by stellar winds from the bubble insides, we computed the expected CO line ratios at different gas temperatures and densities using the RADEX code. We then determined the CO line ratios

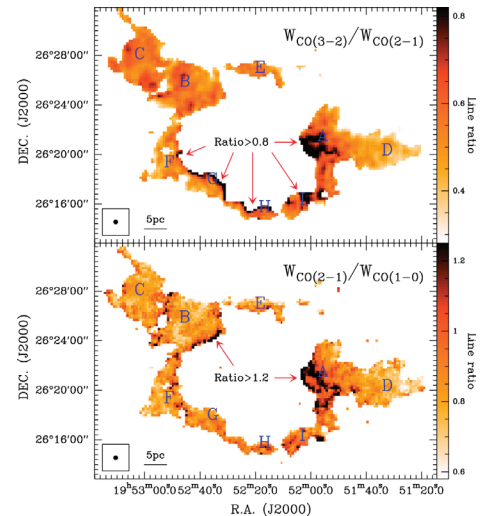


Figure 6: Integrated intensity ratio maps of $W_{\text{CO}(3-2)}/W_{\text{CO}(2-1)}$ (top) and $W_{\text{CO}(2-1)}/W_{\text{CO}(1-0)}$ (bottom) derived from the integrated intensity maps that are above 5σ in Figure 5. The letters indicate the positions of nine molecular clumps (A - I) in the bubble.

that can be used to trace the interactions. In an ordinary molecular cloud, the cold gas is mainly heated by cosmic rays. This heating is balanced by radiative cooling (Draine 2011). As a result, we expect a limited range of temperatures and densities for the molecular gas, which leads to a limited range of observed line ratios. The observed line ratios, which lie far beyond the upper limit, could trace the interaction between the cold and hot gas that presumably lies in the inner rims of a bubble shell because these interactions should increase the temperature and density.

Therefore, we propose to use CO line ratios $W_{\text{CO}(3-2)}/W_{\text{CO}(2-1)} \geq 0.8$ and $W_{\text{CO}(2-1)}/W_{\text{CO}(1-0)} \geq 1.2$ to trace the compressed inner rims of the ring-like shell. The thresholds were selected based on the following considerations. The thresholds correspond to the non-Gaussian tail of the line ratio distribution presented in Figure 7, where we propose that non-interacting clouds should produce line ratios that are Gaussian distributed, and the non-Gaussian parts of the distributions are caused by interaction. To justify our thresholds, we used RADEX to compute the line ratios as a function of gas tempera-

ture and density (see Figure 8). By overlaying the expected range of gas density and temperature found in the most recent numerical simulations (Clark et al. 2012), we derived the expected CO line ratios for non-interacting clouds. The highest ratios are located in regions with moderate or low optical depths ($\tau \leq 5$ for $W_{\text{CO}(3-2)}/W_{\text{CO}(2-1)} \geq 0.8$ and $\tau \leq 1$ for $W_{\text{CO}(2-1)}/W_{\text{CO}(1-0)} \geq 1.2$) in the temperature-density plane. Line ratios higher than this can be used to trace the interaction region where the gas temperature and density are higher than normal.

In summary, we show in Zhang et al (2019) that the high CO line ratios observed ($W_{\text{CO}(3-2)}/W_{\text{CO}(2-1)} \geq 0.8$ and $W_{\text{CO}(2-1)}/W_{\text{CO}(1-0)} \geq 1.2$) are beyond the threshold predicted by numerical simulations based on the assumed density-temperature structure for the inner rims of the ring-like shell, where the compressed areas are located in bubble N131. These high CO integrated intensity ratios can be used as a tracer

of gas-compressed regions with a relatively high temperature and density. This further suggests that the non-Gaussian part of the line-ratio distribution can be used to trace the interaction between the molecular gas and the hot gas in the bubble.

This research is published in Astronomy & Astrophysics (Zhang, et al., 2019) and can be found at <https://ui.adsabs.harvard.edu/abs/2019A%26A...631A.110Z/abstract>.

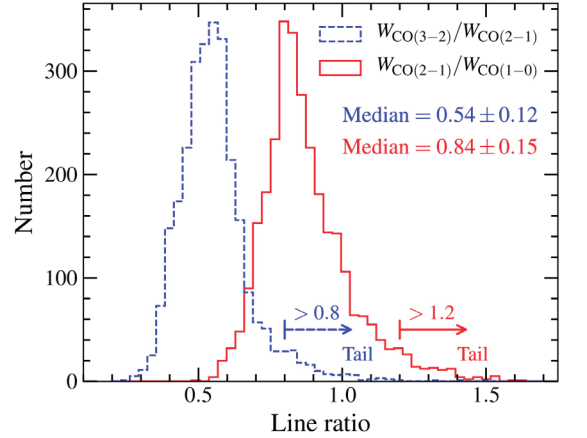


Figure 7: Integrated intensity ratio histograms of $W_{\text{CO}(3-2)}/W_{\text{CO}(2-1)}$ and $W_{\text{CO}(2-1)}/W_{\text{CO}(1-0)}$ for all pixels in Figure 6. The median uncertainties are derived from the standard deviation of the sample.

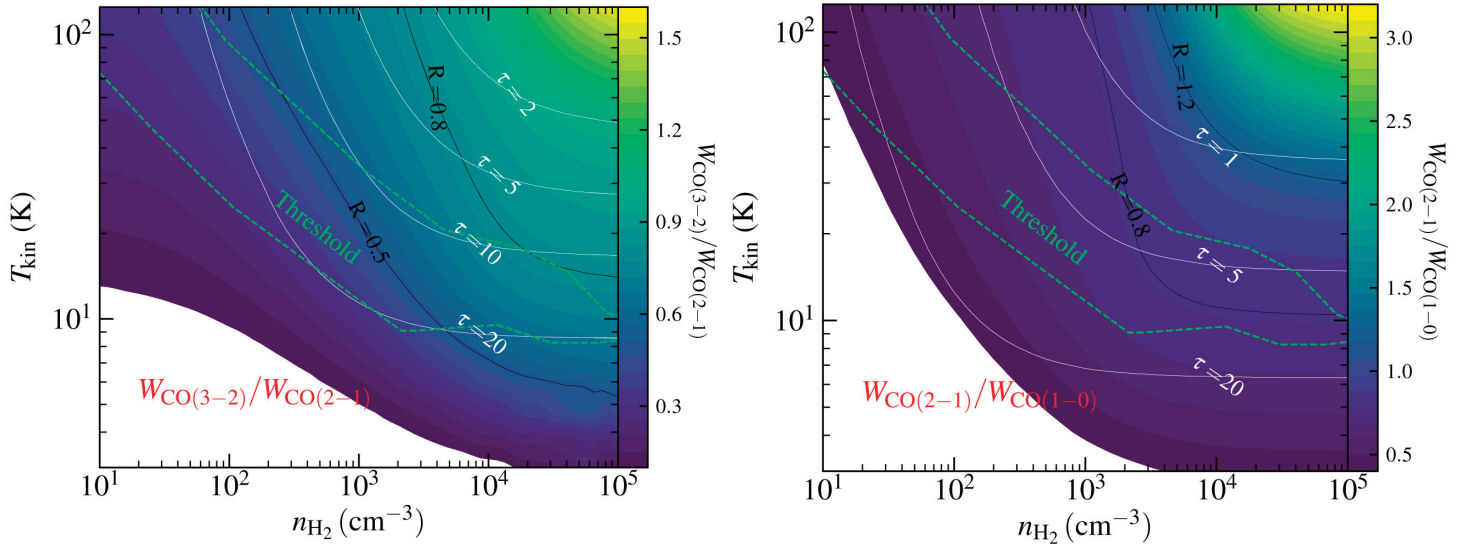


Figure 8: Left: Line ratios $R = W_{\text{CO}(3-2)}/W_{\text{CO}(2-1)}$ and optical depths (τ) CO(2-1), Right: Line ratios $R = W_{\text{CO}(2-1)}/W_{\text{CO}(1-0)}$ and optical depths (τ) CO(1-0) in the conditions of $N_{\text{CO}} = 2.2 \times 10^{17} \text{ cm}^{-2}$ and $\delta v = 3.5 \text{ km/s}$ (estimated by median values in N131) as a function of kinetic temperature and volume density by RADEX modeling. The green contour indicates a region (or threshold) for a possible gas temperature-density distribution in a colliding flow at the onset of star formation from simulations in Clark et al. (2012).

Interplay Between Magnetic Fields, Gravity, Turbulence, and Stellar Feedback in Sh2-201 Revealed by SCUBA-2 and POL-2

Eswaraiah Chakali, National Astronomical Observatories Chinese Academy of Sciences (NAOC), China

The magnetosphere of our earth is enveloped by a bow-shock, which shields our mother earth from the energetic particles emanated from the Sun. Similarly, just outside the heliopause, the solar system is also encompassed by a bow-like shock. Such a bow-shock can effectively shield our solar system from the interstellar wind and cosmic rays. In this regard, it is intriguing to pose a question, is there any astrophysical system, particularly in star-forming regions, where magnetic fields configured into bow-like morphology? If so, what kind of role do they play?

Recently we have found an evidence for such a bow-like morphology of magnetic fields in the dense, massive clumps formed at the waist of a bipolar H II region Sh2-201. In this work we show that bow-like magnetic fields become stronger and shield the massive clumps from erosion by the impact of H II region, reduce the shock strengths induced by the expanding ionization fronts, and stabilize the clumps from gravitational collapse thereby prolonging the star formation. We have used the JCMT, equipped with the sensitive camera and polarimeter

SCUBA-2/POL-2 mounted on the SCUBA-2 camera, and performed high resolution (14" ~ 0.14 pc at 2 kpc), dust continuum polarization observations at 850 μm . These observations enable us to probe the orientation of magnetic field lines within the two massive clumps of S201, lying at different evolutionary stages.

Massive stars (with mass $> 8 M_{\odot}$) can impact their natal molecular clouds through energetic jets and outflows, stellar winds, radiation pressure, H II regions, and supernova explosions. These are collectively known as stellar feedback, which drive energy and momentum into the ambient medium and as a result can trigger or inhibit the second generation of star formation. However, the ultimate outcome of star formation involves the role of various key agents such as gravity, magnetic fields, and turbulence, and stellar feedback. Because, measuring of magnetic fields is difficult in comparison to the other parameters, the relative importance of magnetic fields and the complex interplay among these parameters is not well understood.

Recently, *Spitzer* and *Herschel* observations at mid-infrared, far-infrared, and sub-millimeter wavelengths have shown that bipolar H II regions tend to host massive and compact clumps at their waists. These clumps are the potential sites for the second generation of stars. Therefore, such regions are the ideal laboratories to understand the interplay among the various key parameters and, especially, the role of magnetic fields and their importance in the formation and evolution of massive clumps, star formation in them, and also the formation and evolution of bipolar H II regions themselves. We have studied one

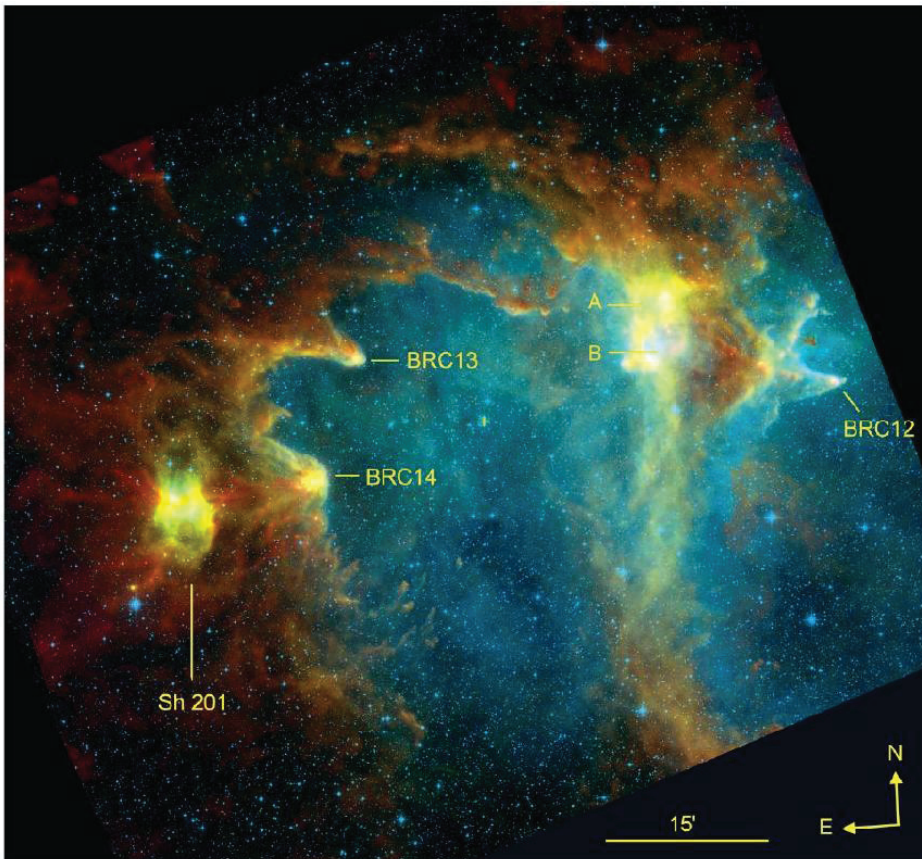


Figure 9: The overall view of the W5-E complex and S201 region. Background image is the color composite of *Herschel* SPIRE/250 μm (red; traces cold dust emission), *Herschel* PACS/100 μm (green; traces warm dust, mainly from the photodissociation regions (PDRs)), and DSS2-red survey (blue; traces $\text{H}\alpha$ emission) images. Various known Bright Rimmed Clouds (BRCs) are shown. This figure is reproduced from Figure 2 of Deharveng et al. (2012, *A&A*, 546, 74) with permission.

such bipolar H II region, Sh2-201 (S201), located at a distance 2 kpc from the Sun and is part of a large molecular cloud complex W5-E (shown in Figure 9).

Sh201 is made up of two lobes extending from the center of the H II region and two dense clumps formed at its waist. We have performed dust continuum polarization towards these two clumps (namely, clump 1 and clump 2) of S201 using POL-2 (project code: M17BP041; PI: Eswarajah Chakali) on 2017 November 18 using POL-2 DAISY mapping mode under JCMT Band 1 weather conditions. With a total integration time of ~ 1.5 hr, we achieved the sensitivity in the intensity map (with pixel size of $12''$) as ~ 5 mJy beam $^{-1}$. We obtain a total of 62 polarization measurements satisfying the criteria of $I/\sigma_I > 10$ and $P/\sigma_P > 2$.

Dust grains are shown to be aligned with respect to the magnetic fields via the “radiative alignment torque” (RAT) mechanism. According to the RAT model, aspherical dust grains rotate as a result of radiative torques imparted by their local radiation and align themselves with their long axis perpendicular to the ambient magnetic fields. The polarized dust emission yields two important quantities – the polarization fraction and the polarization angle – which respectively reveal polarizing dust grain properties and the plane-of-the-sky component of magnetic field orientation. By applying a correction of 90° to the polarization angles, we infer the magnetic field orientation.

Magnetic field geometry is superimposed on the color composite of POL-2 Stokes I, *Herschel*/SPIRE 250 μm , and *Herschel*/PACS 70 μm images shown in Figure 10. Red and gray contours correspond to the distributions of dust emission (based on POL-2 850 μm I map) and of the HII region (based on VLA 1.45 GHz/21 cm continuum), respectively. Evidently, magnetic fields in clump 1 follow a bow-like morphology and are conspicuously compressed at the interface zone between the

dust emission and the ionized medium. This interaction can be witnessed from the closely spaced radio as well as dust emission contours. Magnetic fields also seem to be compressed in clump 2 but with a lower degree of curvature. Based on the correlation between the intensity gradients of VLA 21 cm and magnetic fields, we posit that magnetic fields are shaped by the expanding ionization fronts from the H II region. The range of magnetic field position angles in clump 1 is higher than that in clump 2, signifying the degree of bent is relatively higher in clump 1 than in clump 2, in accordance with the impact of ionized medium. The observed bow-like morphology of magnetic fields in clumps is consistent with 2D magnetohydrodynamic (MHD) and 3D Radiation MHD (RMHD) simulations.

We have utilized the POL-2 Stokes I map, *Herschel* column density, and dust temperature maps to estimate the mass, column density, and number density; and JCMT HARP C ^{18}O (3-2) data were used to derive gas velocity dispersion for the two clumps. Generally, the Davis-Chandrasekhar-Fermi (DCF) method can be employed to sets of Gaussian-distributed polarization angles with angular dispersions less than 25° to estimate the strength. However, magnetic fields in regions altered by H II regions or dragged by gravity will generally exhibit multiple components, and so have significantly higher angular dispersions as in S201. Therefore, we employed an alternative methods such as angular dispersion function (ADF) and auto-correlation function (ACF) analyses to extract the turbulent to ordered magnetic field strength ratios. These values, along with number densities and gas velocity dispersions, are used in the modified DCF relation and estimate magnetic field strengths as 266 ± 32 μG and 65 ± 6 μG for clumps 1 and 2, respectively. In the perpendicular field case with respect to the propagation of ionization-fronts, the magnetic fields get amplified directly upstream of the cloud where the flow stagnates against it, where pressure

and tension in field lines continue to build. The magnetic field strength in clump 1 is larger by a factor of ~ 4 than that in clump 2. Enhanced magnetic field strength in clump 1 is due to relatively more impact of thermal pressure on clump 1.

Using the above parameters, we estimate magnetic and turbulent pressures, and Alfvénic Mach number. In addition, we estimate electron thermal pressure and radiation pressure values, respectively, using radio continuum data from VLA 21 cm/1.4 GHz data and knowing the spectral type of ionizing source as O6V. Comparison between magnetic and turbulent pressures, and Alfvénic Mach numbers suggest that magnetic fields dominate in clump 1 and hence turbulent motions are sub-Alfvénic in clump 1, whereas in clump 2 the gas motions are super-Alfvénic as turbulence dominates over magnetic fields. Comparison between magnetic, turbulent, and thermal pressures in two clumps suggests that dominance of magnetic pressure can reduce the impact of thermal pressure on the clumps by reducing (i) shock strength, (ii) turbulence, and (iii) destructive hydrodynamic instabilities. In contrast, due to relatively weaker magnetic fields in clump 2, the thermal pressure dominates in clump 2 and hence can not reduce turbulence.

The estimated mass (M , 191 M_\odot and 30 M_\odot for clump 1 and 2) to virial mass ratios, $R_{\text{vir}} = M/M_{\text{vir}}$ (where M_{vir} is virial mass estimated based on the balance between gravitational potential and kinetic energies but without considering the supports from magnetic fields and external gas pressure, and are found to be 50 M_\odot and 40 M_\odot) suggest that clump 1 is gravitationally bound and clump 2 is not. Similarly, the critical mass ratios $R_C = M/M_C$ (where M_C is the critical mass that can be supported by the combined contributions from turbulence and magnetic fields, and is found to be 78 M_\odot for clump 1 and 48 M_\odot for clump 2) suggest that clump 1 is under collapse because the support rendered by

turbulence and magnetic fields is not sufficient counteract gravity. In contrast, these factors dominate over gravity in clump 2, and hence is stable. This picture is in accordance with different star formation activity that a larger number of Class 0 and I sources were found in clump 1 signifying active star formation in it, whereas clump 2 is inactive without hosting protostars.

Bipolar bubbles are generally shown to form due to the anisotropic expansion of ionization fronts in a filament. Presence of magnetic fields, oriented perpendicular to the long axis of the filament, would introduce an additional anisotropic pressure to the expanding ionization fronts so as to accelerate the formation process of bipolar bubbles. In addition, as the expansion of H II region proceeds in the filament ridge, gas and dust will be swept up, and as a result, the accumulated material leads to form the dense clumps at the waist of the H II region. It should be noted here that the magnetic field strength will also get enhanced due to continuous compression and flux freezing, as witnessed at least in clump 1. Therefore, gas and magnetic pressures, and hence the total internal clump pressure, will increase with respect to time. Eventually, at a certain point of time, the enhanced clump pressure stops the further expansion of the I-front into the clump. For this to occur, a near pressure equilibrium must be achieved between clump internal (magnetic + turbulent + gas thermal pressures) and feedback (electron thermal + radiative pressure) pressures. We found that clump internal pressure dominates over feedback pressure in clump 1, hence it stops further expansion of the ionized region, whereas feedback pressure is nearly in equilibrium with the pressure in clump 2.

Our analyses show that magnetic pressure dominates over thermal pressure (at least in clump 1), and that magnetic fields within the clumps situated at the waist of the H II region can constrain the paths of I- front blowing away from the filament ridge. We evidenced that

enhanced magnetic fields not only guide the ionized gas and aid the formation of bipolar H II regions but also shield the clumps from erosion. Furthermore, these signatures imply that the enhanced magnetic fields and turbulence in the clumps can counteract gravitational collapse and hence delay the evolution of the clumps hence the star formation.

Based on our analyses, we posit that feedback from the H II region has the following consequences: it (a) causes the formation of clumps in the filament ridge, i.e., at the waist of the HII region and (b) enhances the magnetic field strength in the clumps and injects turbulence into the clumps, and (c) eventually, the enhanced magnetic fields will

be able to shield the clumps from erosion and so govern their stability, guiding the I-fronts to be blown away from the filament ridge, and aiding in the formation of bipolar H II regions. Therefore, magnetic fields can play a crucial role not only in the formation and evolution, and star formation in the massive clumps, but also in governing the feedback processes.

This research is published in *Astrophysical Journal* (Eswaraiah, Di, Samal et al. 2020, *ApJ*, 897, 90). Open version of the paper can be found at <https://ui.adsabs.harvard.edu/abs/2019arXiv191210188E/>.

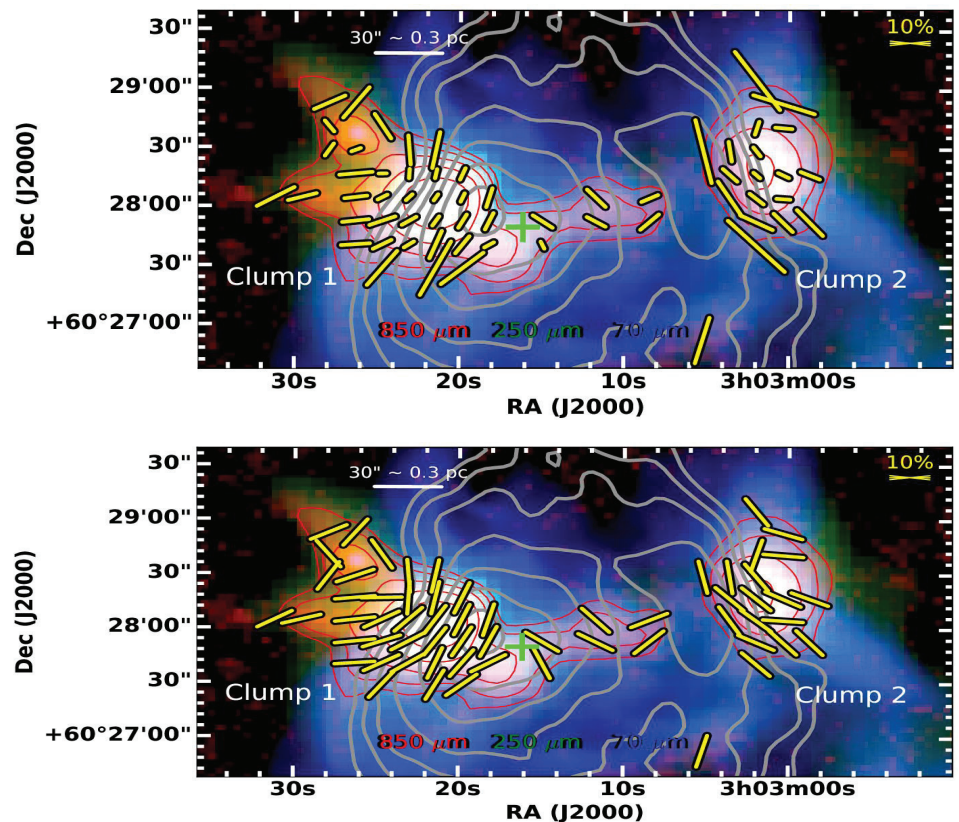


Figure 10: Vector maps showing magnetic field orientations, lengths proportional to polarization fraction (top panel) and with fixed lengths (bottom panel). magnetic field vector maps are overlaid on the color composite of POL2 850 μm Stokes I (red), Herschel SPIRE/250 μm (green), and Herschel PACS/70 μm (blue) images. Red and gray contours are correspond to POL2 850 μm Stokes I and VLA/21 cm continuum emission maps, respectively. In both panels, reference vectors with a magnetic field orientation of 90° are shown. For more details see Eswaraiah et al (2020, *ApJ*, 897, 90).

First Sub-pc Scale Mapping of Magnetic Fields in the Vicinity of a Very Low Luminosity Object, L1521F-IRS

Archana Soam, NASA Ames Research Center, USA

Magnetic fields in star-formation

Magnetic fields (B-fields) are found to be one of the important drivers in the star formation process but they are not very well constrained by available observations. The influence of B-fields on various spatial scales and stages of star-formation is still unclear. Both magnetically dominated and turbulence dominated scenarios have been advocated to explain the fact that star formation is slow compared to free-fall times. In the magnetically dominated scenario for isolated low mass star formation, the cores gradually condense out of a magnetically subcritical background cloud, through ambipolar diffusion. In this process, the material, mediated by the magnetic field lines, settles into a disk-like morphology of a few thousand AU in size. This allows the cloud-scale magnetic fields to become parallel to the cloud minor axis. Turbulence-dominated scenarios will produce less orderly magnetic field configurations.

The core

L1521F is located in the Taurus star-forming region at a distance of 140 pc. This core contains a very low luminosity object (VeLLO) L1521F-IRS with bolometric luminosity of $L = 0.05 L_{\odot}$. The embedded VeLLO L1521F-IRS is found to be associated with a compact but poorly collimated molecular outflow in CO(J=2-1) line observations. However, a very compact bipolar outflow centered at L1521F-IRS is found from HCO⁺ (J=3-2) ALMA observations. Figure 11 is taken from Takuda et al. based on their molecular line observations of this core. This drawing shows starless cores in the vicinity of L1521F main core which exhibits very compact bipolar outflows. There is an interesting arc-like feature in HCO⁺ emission suggesting a highly dynamical star-formation process.

Magnetic fields in L1521F

The field geometry in L1521F envelope seen from optical observations are zoomed in panel (b) of Figure 12. The mean orientation of field lines is from north-east to south-west directions which seems consistent to that seen in Planck observations. The field lines appear organized but not aligned with the outflow direction. The B-field geometry is investigated in L1521F from POL-2 850 μ m observations by further zooming-in (panel (c) of figure 12). Interestingly, the north-east to south-west component is still seen in the map. The difference between the outflow direction and the magnetic field orientation in the envelope is $\sim 50^{\circ}$. The core scale B-fields are also misaligned with an offset of $\sim 48^{\circ}$ between outflows and mean magnetic field orientation. However, field lines are more aligned with outflows if the north-eastern component only is taken into account. The maps seen at three different scales and core scales are connected and the global B-field orientation is from north-east to south-west. An interesting feature of bending in field lines can be seen in the core scale B-field geometry. This is further demonstrated in Figure 13 where elliptical core and the field lines are shown. The location of embedded source in the core is shown with a star symbol. The associated bipolar outflow cavities are indicated with dashed parabolas based on the Spitzer observations of this source shown in color-composite image as inset in the upper-right corner of this figure. The field lines in this cartoon seem to be result of north-east

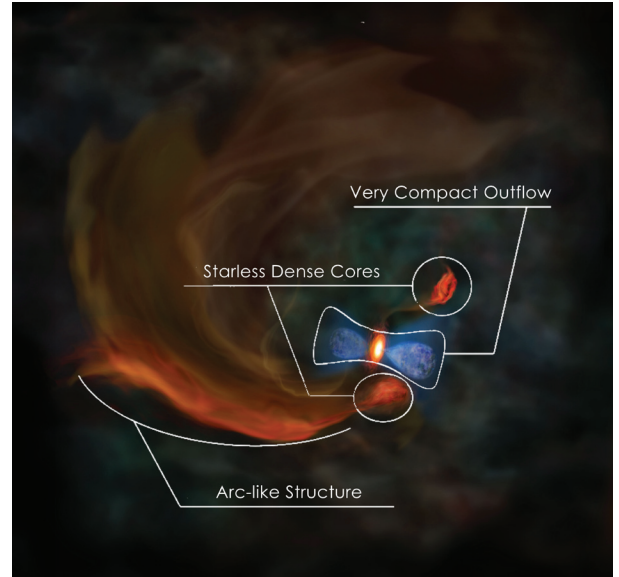


Figure 11: An artist's conception of the center of a molecular cloud core MC27 based on the ALMA observation results with descriptions of each component. This figure is adapted from the Takuda et al. (2014) poster with Credit to NAOJ

to south-west orientation of Planck and optical polarization observations which gets bent in core seen as submm wavelength. we used a modified version of the Davis-Chandrasekhar-Fermi technique to measure the plane-of-the-sky (B_{pos}) strength of magnetic fields as 330 μ G in the core and 25 μ G in the envelope of L1521F.

Mass-to-flux ratio and energy budget of the core

We considered values of B_{pos} and column density to calculate the mass-to-flux ratio of $\lambda = 2.3 \pm 0.7$ which suggests that the core is super-critical and consistent with the asymmetric line-profiles seen in global infall motions. The calculated magnetic energies in the envelope and core are 1-2 orders of magnitude higher than the non-thermal kinetic energies of these regions suggesting that magnetic fields are more important than turbulence and contributing more to the energy budget of L1521F.

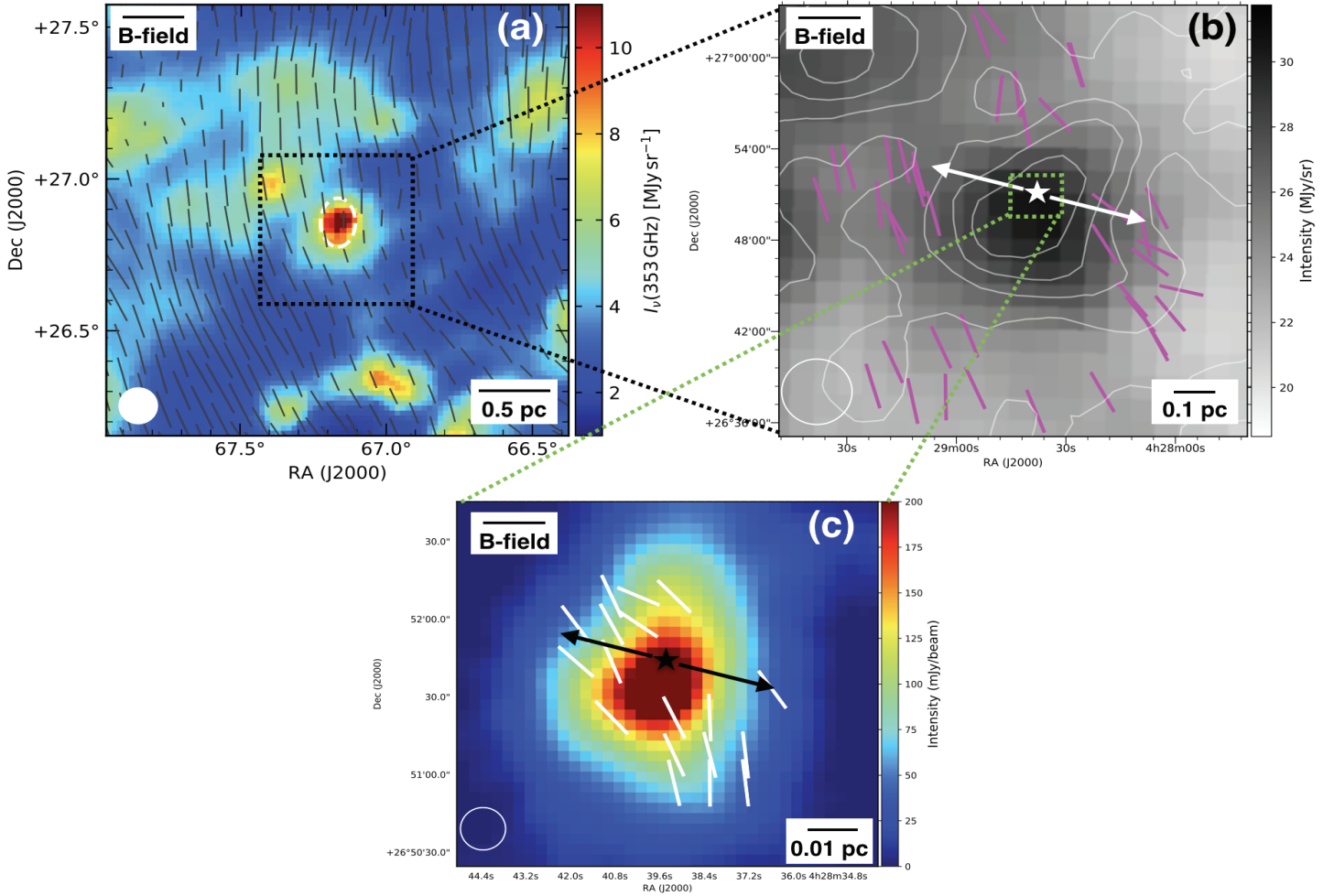


Figure 12: Panel (a): Morphology of B-fields obtained from Planck 850 μm dust polarization observations. The location of L1521F is shown with dashed ellipse in the center. Panel (b): The B-fields mapped with optical R-band (0.63 μm) observations by [1] plotted on IRAS 100 μm with the contours of Dobashi extinction map of L1521F ([2]). The position of VeLLO and associated CO bipolar outflows ([3]) are shown with star symbol and double headed arrow. Panel (c): The B-field morphology obtained from 850 μm dust polarization observations of L1521F core shown on 850 μm dust continuum map. The lengths of line-segments are normalized and independent of fraction of polarization. The beam sizes in all the frames are shown with filled and open circles.

Depolarization in the core

We investigated the change in polarization fraction from diffuse to high density regions on L1521F core as done in several other star-forming regions. We measured the power-law slope in the distribution using a least-squares fit, and found it to be $\alpha = -0.86$. The widely accepted possible reasons of lower observed polarization fraction in the cores include the changes in B-field orientation in the denser regions. These changes could also stem from the grain growth with a consequence of more spherical shapes thus not getting aligned with the B-fields. Other possible reasons of the change are suspected to be the magnetic reconnection and from weak Radia-

tive Alignment Torques due to weak radiation field in dense regions. But the radiation from L1521F-IRS may compensate for the loss of interstellar radiation field and help in radiative alignment of the grains.

This research is published in the Astrophysical Journal (Soam et al. 2019 ApJ. 883:9) in September 2019 and was conducted at SOFIA Science Center (USRA), NASA Ames, USA. The project was started in 2018 at Korea Astronomy & Space Science Institute (KASI), South Korea. An open access version of the paper is available at <https://arxiv.org/abs/1908.01018>.

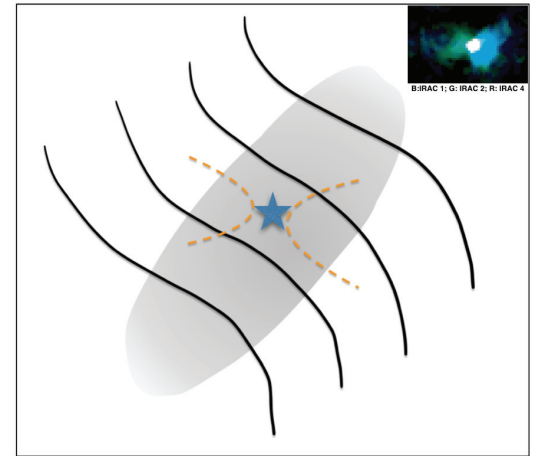


Figure 13: Cartoon showing the field lines, location of L1521F-IRS and bipolar outflow cavities in L1521F. The inset in upper right corner shows the Spitzer color composite image.

Betelgeuse Was Not Fainter Because of Dust

Thavisha Dharmawardena, Max Planck Institute for Astronomy, Taiwan/Germany; Steve Mairs, Senior Scientist, EAO/JCMT; Peter Scicluna, European Southern Observatory, Taiwan/Chile

Earlier this year, Betelgeuse took the media by storm after a record-breaking dimming at visual wavelengths. This surge of public interest was largely fuelled by exaggerated claims of the red supergiant's impending demise, though several experts opined that the dimming was likely not a precursor to an imminent supernova explosion. Regardless of the ultimate fate of Orion's shoulder, the dimming event was obviously worthy of investigation for the potential implications of evolved stellar evolution and the surrounding environment of the massive star. While the dominant narrative in the literature suggested that the dimming was due to a newly formed dust enhancement in the line of sight to the star (Levesque & Massey 2020), new JCMT/SCUBA-2 submillimetre observations also show a dimming, suggesting the change in brightness was not due to dust, but a change in the photosphere of the star, itself.

Betelgeuse is the nearest red supergiant star to the Earth at a distance of only 152 ± 20 pc (van Leeuwen, 2007). With such a close proximity, it acts as a unique laboratory to aid in the understanding of the late stages of red supergiant evolution. Massive stars ($M > 8M_{\text{sun}}$) are important to study as they are the main drivers of chemical evolution in the universe (Karakas & Lattanzio 2014). Even before the explosive end of their lives, stars like Betelgeuse undergo significant mass loss, enriching their environment with newly formed elements. While the evolution of mass loss during these phases is critically important in understanding the final stages of a star's life and what type of supernova will eventually occur (e.g. Georgy 2012; Groh et al. 2013), the driving forces behind the mass loss episodes are still under active investigation. Radial pulsations with periods of up to a few years, however, clearly play a role in at least some cases (e.g. van Loon et al.

2005; Harper et al. 2009) and their semi-regular variations are tracked by optical and near infrared fluxes.

Beginning in October, 2019, Betelgeuse experienced an unprecedented V band dimming of >1 mag (a factor of ~ 3 change in brightness; see top panel of Figure 14) during one of its regular pulsation cycles.

A variety of explanations were proposed to explain this phenomenon such as: 1. A confluence of the star's short (~ 400 days) and long (~ 5 years) variation periods, 2. Changes in known hot and cold spots on the stellar surface, 3. Photospheric structural changes indicating an imminent supernova (which is now ruled out by the star's return to its original

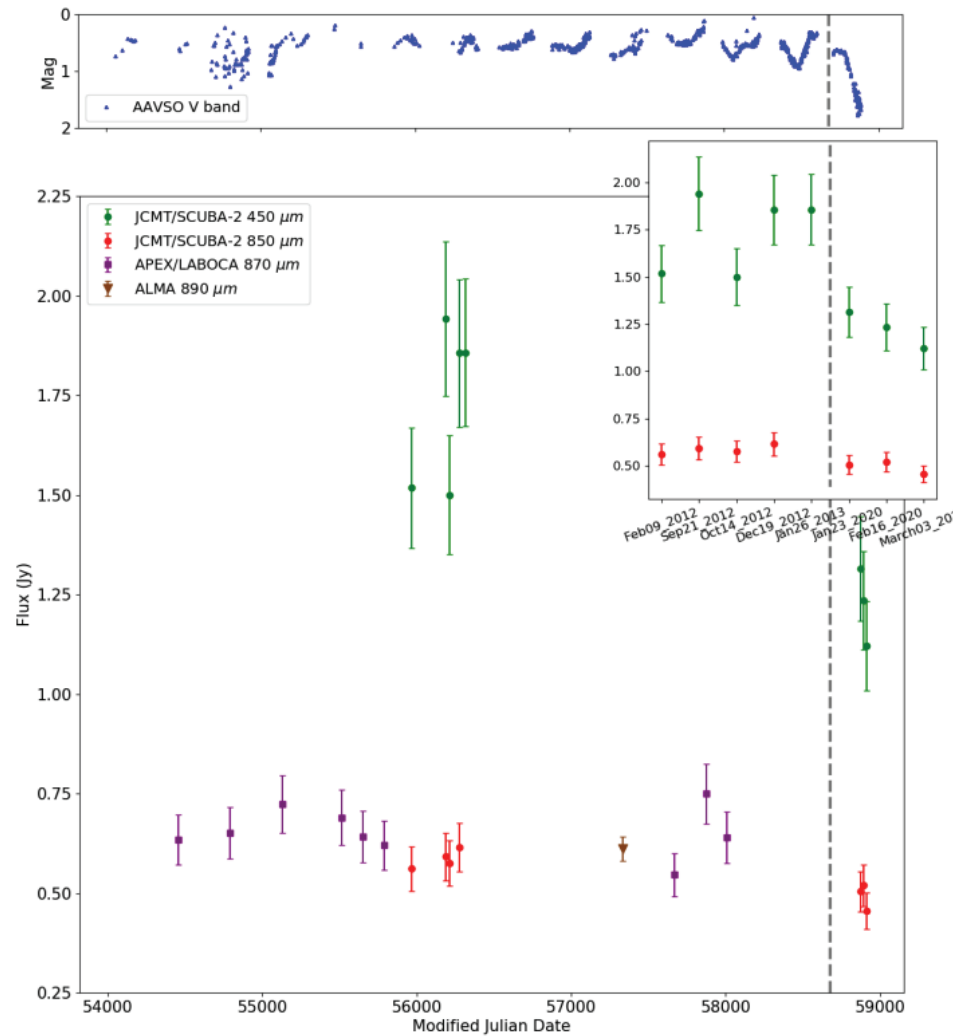


Figure 14: From Dharmawardena et al 2020. Lightcurves of Betelgeuse for the last fifteen years: The top panel shows the AAVSO optical (V band) light curve; The bottom panel shows the JCMT/SCUBA-2 450 μm (green points) and 850 μm (red points) light curve. The APEX/ LABOCA 870 μm light curve (purple squares) was obtained from archival data. Also shown is a single ALMA 890 μm data point (brown triangle) from O’Gorman et al. (2017), to illustrate the consistency. The grey dashed line indicates the beginning of the dimming of the recent pulsation cycle. The inset panel shows a zoomed in version of the JCMT/SCUBA-2 light curve with the corresponding UT date for each observation.

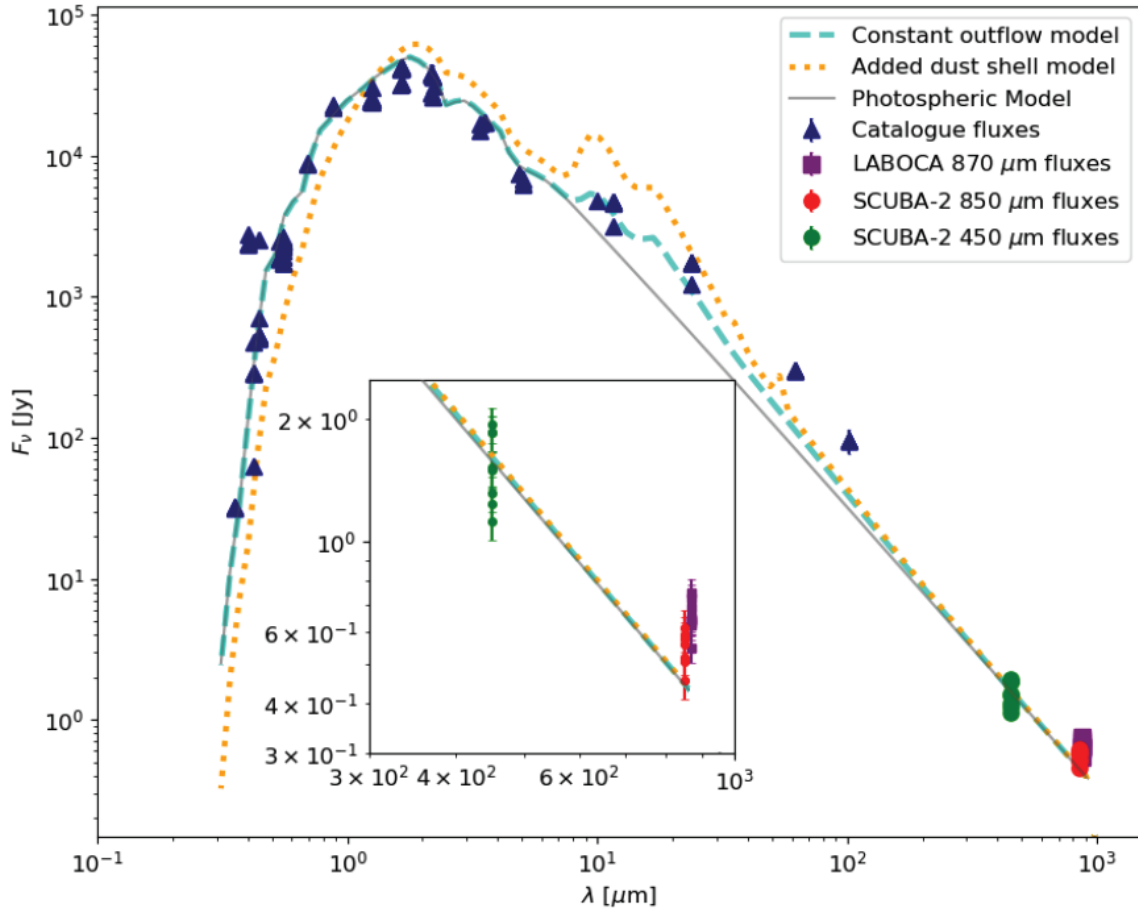


Figure 15: From Dharmawardena et al 2020. Radiative-transfer models (lines) compared with observations of Betelgeuse. Blue triangles show fluxes, taken from Vizier (see Dharmawardena et al 2020 for more details), and the green, red and purple points indicate the submillimetre data at 450, 850, and 870 μm , matching Figure 14. The blue dashed line represents a qualitative fit from Hyperion to the 0.3 – 30 μm photometry, and the orange dotted line a model that is identical other than the addition of an extra shell of dust from 2 – 4 R_{\star} . The grey solid line shows the underlying photospheric model at the same spectral resolution as the radiative-transfer models. The inset panel highlights the submillimetre fluxes.

brightness), and 4. A large ejection of newly formed dust along the line of sight. The latter emerged as the most favourable explanation based on optical spectrophotometry.

The dust emission at SCUBA-2’s operating wavelengths (450 and 850 μm) is optically thin. Therefore, if the dimming of Betelgeuse truly was due to a newly formed dust cloud, we would expect to see either a constant submillimetre flux before and during the event or, perhaps, a slight increase in the flux during the optical dimming. Regardless, an increase in the dust mass cannot decrease the submillimetre flux. Both archival and newly obtained SCUBA-2 continuum data at 450 and 850 μm were used in conjunction with Apex/LABOCA (870 μm) data to investigate this hypothesis. At these wavelengths, we avoid

the effects of extinction along the line of sight, providing an unbiased probe of the emission of the star and its environment. The LABOCA data was obtained in two epochs between 2007-2011 and 2016-2017 while archival SCUBA-2 data was obtained in 2012-2013. The pre-optical dimming (2012-2013) SCUBA-2 850 μm fluxes are consistent with those derived by O’Gorman et al. (2017) using the ALMA main array at a wavelength of 890 μm . New SCUBA-2 observations were obtained using Director’s discretionary time and a follow-up urgent queue program resulting in three observations in January, February, and March 2020 (during Betelgeuse’s optical dimming). A cursory look suggested the newly obtained submillimetre data appeared to be fainter than the archival data.

To statistically verify whether there was indeed robust evidence of variation at submillimetre wavelengths, Bayesian inference by forward modelling was employed. Three models were constructed: 1. The “Constant flux model”, where the 450, 850, and 870 μm data remained constant over the whole light curve, 2. The “two epoch model”, where the behaviour is broken into two distinct epochs (pre- and during optical dimming), each with constant, but different flux, and 3. The “linear flux variation model”, where fluxes are proportional to $mt+c$, where each wavelength follows the same slope, m , over time, t . The priors on all free parameters were assumed to be flat, drawn from uniform random distributions.

To compute the evidences for each model, the Python package

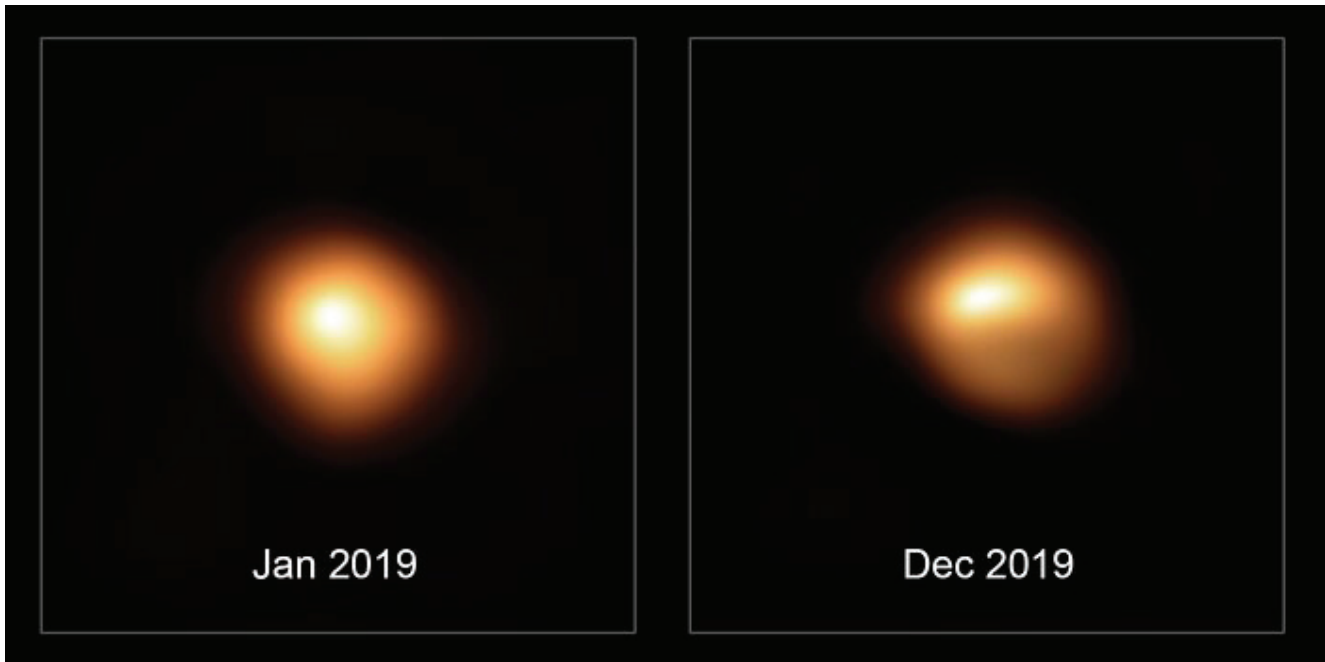


Figure 16: These observations, obtained by the SPHERE instrument on ESO's Very Large Telescope (PI: Montargès), show Betelgeuse before (left) and during (right) its dimming. The irregular brightness across the surface during the dimming in December 2019 is apparent. Credit: ESO/M. Montargès et al.

“Dynesty” was used (Skilling 2004, 2006; Higson et al. 2019; Speagle 2020). The most robust model was found by computing Bayes’ factor (K) for each pair of models. The Bayes’ factor enables the selection of the most appropriate model from a given set by comparing the ratio of evidences (assuming that all models are equally likely, a priori). The Bayesian analysis clearly favoured the “two epoch model” by a wide margin when compared to either of the other two models. This result decisively indicates that the submillimetre flux is variable and that it was fainter during the optical minimum when compared to earlier observations.

Once it was clarified that the decrease in flux was visible over optical through submillimetre wavelengths, dust radiative transfer modelling was performed using the Hyperion Monte Carlo radiative transfer code (Rorbitaille 2011) to robustly disentangle the effects of the flux from a potential dust shell compared to the flux from the photosphere of Betelgeuse at submillimetre wavelengths. Two models were run assuming a spherically symmetric wind with constant outflow speed and a dust model/mass loss rate that matched the optical to mid-infrared photometry. In

one of the two models, however, an additional shell of dust was added between 2 and 4 R_{\star} , creating an optical dimming of ~ 1 magnitude. These models indicate that Betelgeuse’s emission at submillimetre wavelengths is entirely dominated by the stellar photosphere, with only small contributions from circumstellar dust, as expected (see Figure 15). It is therefore clear that only changes in the photosphere can reproduce the observed submillimetre dimming.

The amount of submillimetre dimming implies that the luminosity of Betelgeuse has decreased by nearly 20% (a 3.6σ change) and argues strongly against models in which the optical dimming is caused by the formation of a new cloud of dust along the line of sight to the star. This 20% reduction in luminosity could take the form of a change in radius or temperature. The favoured explanation is an apparent change in temperature attributed to the presence of large star spots. In December, 2019 Montargès et al released high resolution images of Betelgeuse obtained by the SPHERE instrument at ESO’s Very Large Telescope. Figure 16 shows the comparison of Betelgeuse before (January 2019) and during (December 2019)

the dimming event. The irregular surface brightness is apparent. The JCMT and ESO data taken together suggest spots that are ~ 400 K cooler than the surrounding photosphere covering $\sim 50\%$ of the visible surface or spots that are ~ 300 K cooler covering 70% of the surface. Both scenarios replicate the ~ 1 magnitude dimming observed at optical wavelengths.

Soon after the dimming, Betelgeuse began to increase in brightness once more, but instead of returning to its original, expected value, recent observations from the STEREO solar observatory have shown that flux variations continue to be highly unusual (ATel #139011). Over the next year, Betelgeuse’s submillimetre light curve will continue to be monitored monthly with SCUBA-2 as a continuation to the urgent program accepted earlier this year to investigate further photospheric changes.

This research is published in *Astrophysical Journal* (Dharmawardena, Thavisha E. et al. 2020). Open version of the paper can be found at <https://ui.adsabs.harvard.edu/abs/2020ApJ...897L...9D/abstract>

Two Sub-Millimetre Bright Protoclusters Bounding the Epoch of Peak Star-Formation Activity

Kevin Lacaille, Dalhousie University, Canada

In the local Universe, galaxy clusters represent some of the densest environments where mostly passive galaxies reside, with the most massive elliptical galaxies known residing at their centres (Bower et al. 1992). Therefore, massive galaxy clusters must have formed the bulk of their member galaxies' stellar mass at early times (Hopkins and Beacom 2006). At high-redshift, a significant amount of enhancement of star formation is observed in galaxies residing in candidate protoclusters – the progenitors of massive local galaxy clusters (Chapman et al. 2009). Thus, there is some evidence that at high redshift, galaxy evolution is accelerated at early times in regions of strong over-density.

In this study, we observe two galaxy protocluster fields that were uncovered through the identification of redshift over-densities of Lyman break galaxies (LBGs): HS1549 (Steidel et al. 2011) and HS1700 (Steidel et al. 2005). The HS1549 and HS1700 fields contain some of the strongest redshift over-densities found in previous $z > 2$ surveys. In HS1549, the galaxy over-density is even larger than that of HS1700, exhibiting a factor of 13 times that of the field in a volume of $\sim 5000 \text{ Mpc}^3$, and has almost $10\times$ the surface density of Ly α emitters, compared to the average among 20 fields covered to a similar depth, representing one of the richest fields of Ly α -selected objects ever observed, at any redshift. Using SCUBA-2, we detect 56 sub-millimetre galaxies (SMGs) at $850 \mu\text{m}$ over $\sim 50 \text{ arcmin}^2$, covering both HS1549 and HS1700 survey fields, as shown in Figure 17.

We estimate de-boosted cumulative number counts for each protocluster field and when compared to the SCUBA-2 Cosmology Legacy Survey (S2CLS, Geach et al. 2017), the largest $850 \mu\text{m}$ survey to date, we find that over their SCUBA-2 fields, neither HS1549 nor HS1700

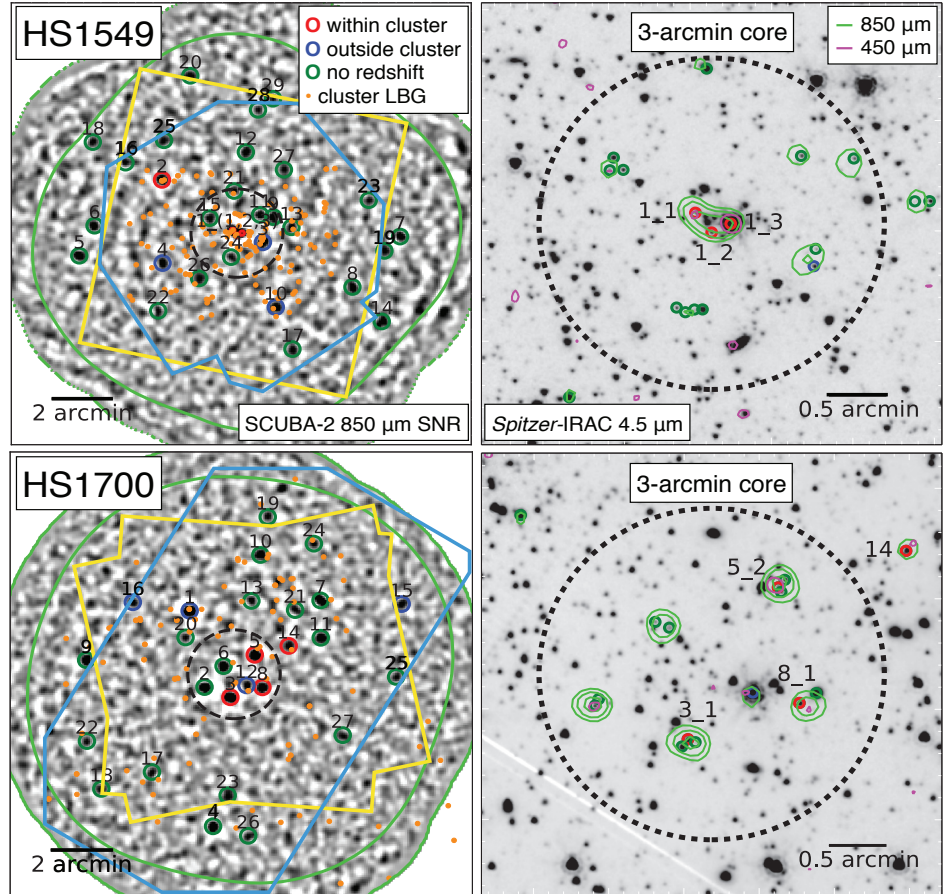


Figure 17: Images of the HS1549 field and the HS1700 field. Left: SCUBA-2 $850 \mu\text{m}$ SNR images. The coloured open circles represent $> 4\sigma$ SCUBA-2 $850 \mu\text{m}$ identified sources. Right: Spitzer-IRAC $4.5 \mu\text{m}$ images of the 3-arcmin core region of each protocluster field. The light green contours of $\text{SNR}_{850} = (4, 7, 11)$ and magenta contours of $\text{SNR}_{450} = 3$.

present any over-density for sources brighter than 4 mJy (see Figure 18), when sampled on the same scale of 12-arcmin diameter ($\sim 6 \text{ Mpc}$ at $z \sim 2.5$). However, the number counts over the 3-arcmin diameter core regions shown in Figure 17, indicate that both fields are significantly over-dense, compared to the average counts of the S2CLS. Our protocluster regions show overdensities within their $\sim 1.5 \text{ Mpc}$ core regions of 6 ± 4 (HS1549) and 4 ± 2 (HS1700).

We analyze the $850 \mu\text{m}$ properties of each protocluster and we have ascertained that the over densities defined from LBG redshift spikes in HS1549 and HS1700, are mirrored in the dusty SMG population, as well. We have spectroscopically con-

firmed that in each protocluster, at least four of these SMGs are at the protocluster redshift, and statistically from the counts (or less robustly with photometric redshift identifications), many other SMGs must lie at the protocluster redshifts. In both protoclusters, the statistically significant SMG over-density is confined to the core ($\sim 1.5 \text{ Mpc}$ diameter) region, consistent with other sub-mm studies of protoclusters that find an overabundance of dusty, luminous galaxies in the cluster core (e.g., Stach et al. 2017).

We combine multi wavelength estimates of the star-formation rates (SFRs) and find total SFRs of $12,500 \pm 2800 \text{ M}_\odot \text{ yr}^{-1}$ ($4900 \pm 1200 \text{ M}_\odot \text{ yr}^{-1}$) in HS1549 (HS1700). Additionally, we

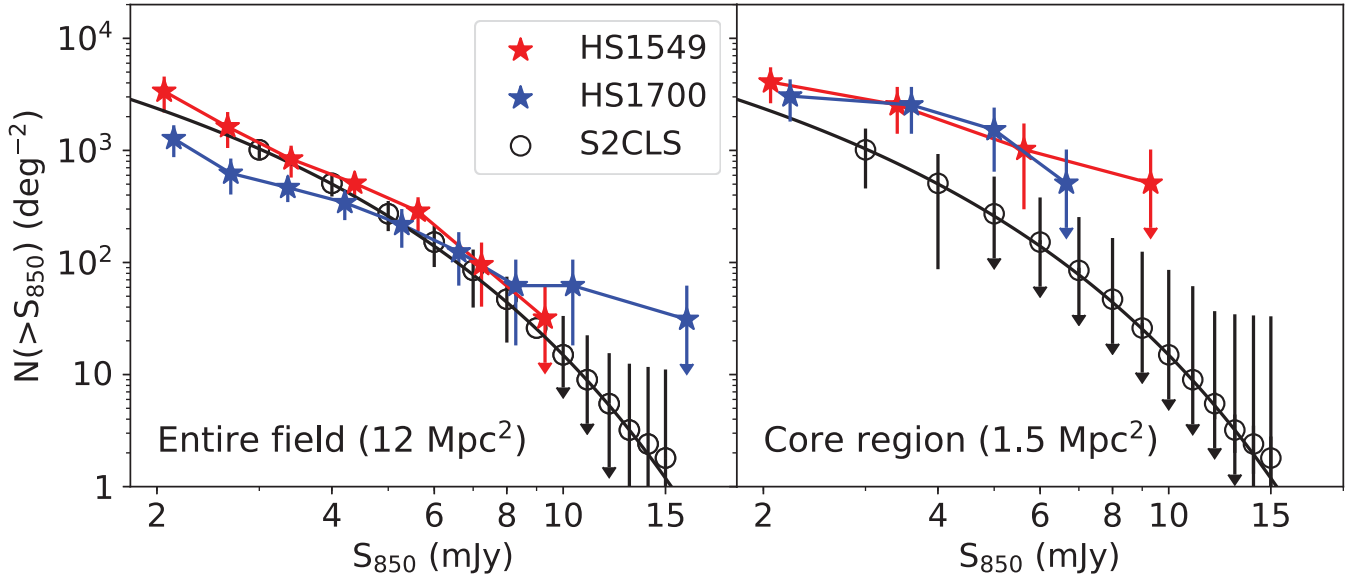


Figure 18: Cumulative number counts of $> 4\sigma$ 850 μm sources for each protocluster's field (left) and 3-arcmin core (right). We find that neither protocluster field is over dense over their entire SCUBA-2 fields, however, the HS1700 field suggests a possible overdensity between 5 – 100 \times for sources brighter than 8 mJy. In addition, we find that both field's ~ 1.5 Mpc core regions show overdensities of $6\pm 4\times$ (HS1549) and $4\pm 2\times$ (HS1700) compared to blank field surveys.

find SFR densities (SFRDs) within the central 1.5 Mpc diameter of each protocluster to be $3000 \pm 900 M_{\odot} \text{ yr}^{-1} \text{ Mpc}^{-3}$ ($1300 \pm 400 M_{\odot} \text{ yr}^{-1} \text{ Mpc}^{-3}$) in the HS1549 (HS1700) protocluster (see Figure 19). These SFRDs are a whopping 10,000 \times larger than the global SFRDs found at their respective epochs, due to the concentration of star-forming galaxies in the small volume of the dense cluster cores.

Recent SCUBA-2 observations of galaxy protoclusters have shown that SMGs in high-redshift galaxy protoclusters tend to be centrally-concentrated and reside in over-dense environments, suggesting rapid galaxy evolution in high-density environments in the early Universe (Casey et al. 2015). Combining SCUBA-2 detected SMGs within the protoclusters and less luminous members we find both protoclusters have large integrated mass-normalized star-formation rates that are consistent with a $\propto (1+z)^7$ trend, suggesting much more rapid evolution compared to an extrapolation of the local field galaxy trend.

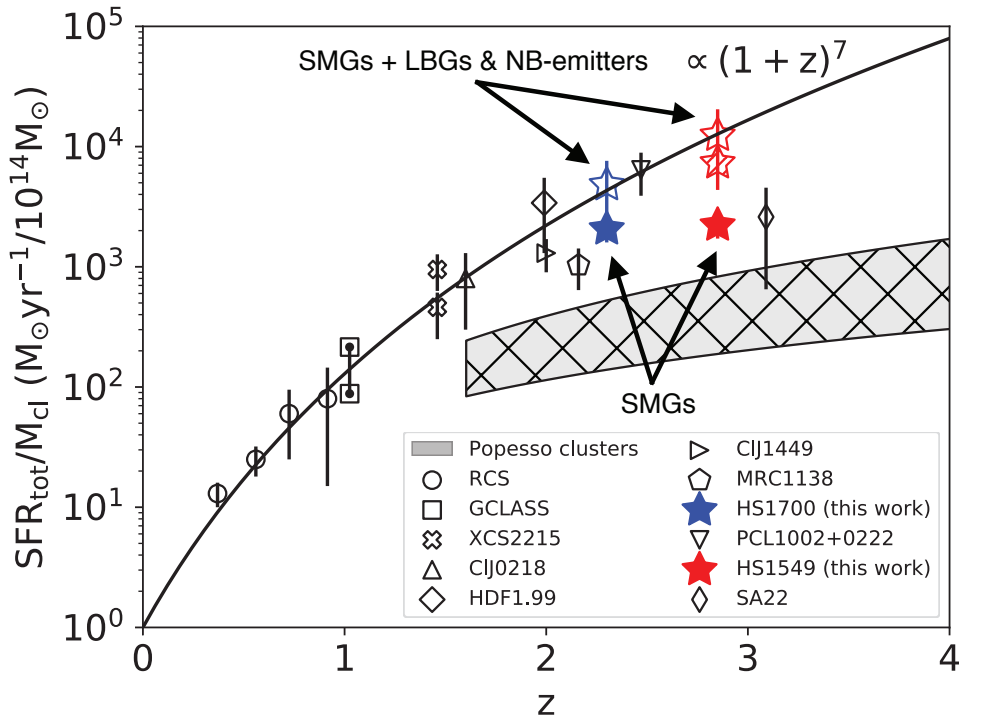


Figure 19: Integrated star-formation rate of galaxy clusters and protoclusters normalized by their total mass as a function of redshift. We compare field galaxy evolution to protoclusters at $z > 1$ and find protoclusters follow a $(1+z)^7$ relation, suggesting much more rapid evolution compared to an extrapolation of the local field galaxy trend.

This research is published in the Monthly Notices of the Royal Astronomical Society (Lacaille,

Kevin et al. 2020). Open version of the paper can be found at

<https://ui.adsabs.harvard.edu/abs/2019MNRAS.488.1790L/abstract>

Dense Molecular Gas and Star Formation in Nearby Galaxies - Recent Results from MALATANG

Xue-Jian Jiang, EAO Fellow, EAO/JCMT

The important role of molecular gas in the star formation process has received much attention from observational and theoretical studies by astronomers. It is found that the change of the molecular-gas fraction (defined as the gas mass per unit stellar mass) over time is surprisingly similar to that of the cosmic star formation rate density, in the sense that they both appear to be higher at redshift $z \sim 1-2$ (~8-11 billion years ago) and decline toward the present Universe. This indicates that throughout most of cosmic time, molecular gas is the crucial fuel for star formation and galaxy evolution. However, there are still some intriguing open questions, such as, how do we interpret the variations observed in the star formation (SF) relationship which relates the rate of star formation (SFR) and the amount of cold gas (Kennicutt–Schmidt law, Kennicutt 1998), and how do the density and temperature of molecular gas relate to the SFR? Since the pioneering studies of Gao & Solomon (2004a, b), it has been shown that the amount of dense molecular gas is tightly and linearly correlated with the SFR of individual galaxies (in logarithmic scale), where dense gas is usually defined as gas with a volume density $> 10^4 \text{ cm}^{-3}$, and can be traced by molecular emission lines with high critical densities like HCN. Meanwhile, observations on smaller physical scales, such as of resolved galaxy structures or of molecular clouds in our Milky Way, also found that star-forming sites are mainly associated with dense structures (Wu et al. 2005). Due to the complex nature of interstellar molecules, multiple transitions, especially high- J lines, are necessary for a more robust analysis of the relationship between dense gas tracers and SF.

To bridge the gap between Milky Way clouds and galaxy-integrated observations, and to explore the re-

lationship between dense gas and star formation in nuclear versus disc regions of galaxies systematically, the MALATANG (Mapping the dense molecular gas in the strongest star-forming galaxies) large program has been carried out on the JCMT. It is the first systematic survey of the spatially resolved HCN $J = 4-3$ and $\text{HCO}^+ J = 4-3$ emission in a sample of nearby galaxies. The HARP receiver provides high spatial resolution and multiple beams for quick survey speed. Ancillary archival data of CO 1–0, CO 3–2, infrared imaging data from *Spitzer* (IRAC 3.6 μm and MIPS 24 μm) and *Herschel* (PACS 70, 100, and 160 μm) were obtained for a more comprehensive analysis of the interstellar medium.

The team explored the relationship between the dense gas and

the SFR and show that the power-law slopes are close to unity over a large dynamical range (Figure 20). Moreover, the variation of this relationship could be dependent on the dense-gas fraction (f_{dense}) and dust temperature (Tan et al. 2018; Jiang et al. 2020).

The published MALATANG paper by Jiang et al. (2020) carefully analyzed NGC 253 as a case study. For this nearest circumnuclear starburst galaxy, they explore the relationship between different kinds of molecular gas, SF, and stellar components. The higher observed transitions have provided important information on the truly dense gas close to the galaxy center.

Both HCN 4–3 and HCO^+ 4–3 show more concentrated emission mor-

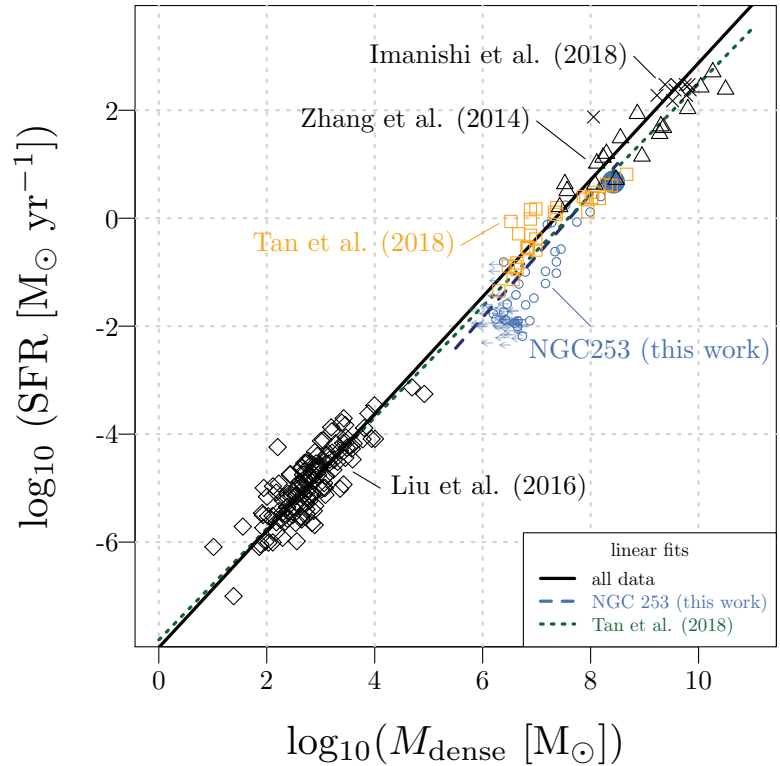


Figure 20: Dense-gas star formation relationships (SFR versus M_{dense}) for all HCN 4–3 samples compiled in this work. The black solid line is a linear fit (in logarithmic scale) for all data ($\beta = 1.08 \pm 0.01$). The blue dashed line is a fit for NGC 253 data ($\beta = 1.13 \pm 0.14$). The dotted line is the fit ($\beta = 1.03 \pm 0.01$) from Tan et al. (2018).

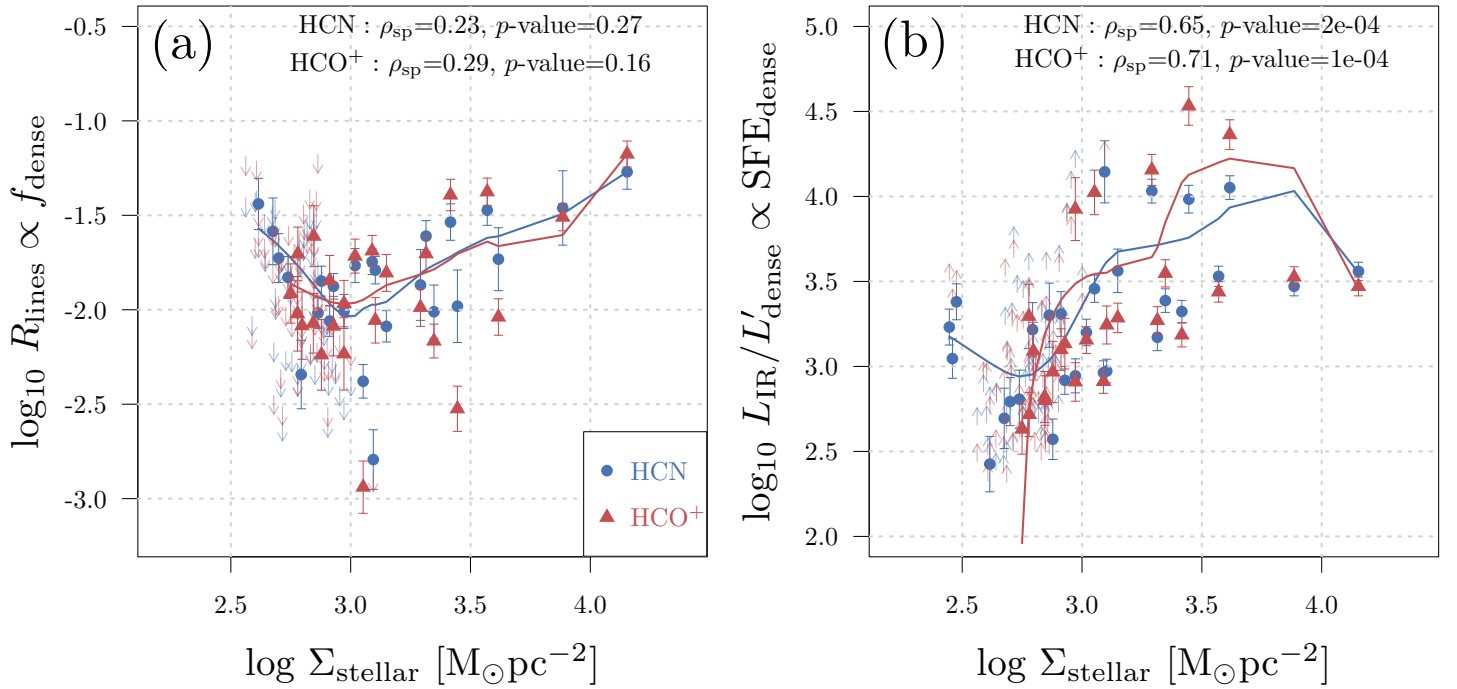


Figure 21: Left: f_{dense} as a function of stellar surface density Σ_{stellar} . Right: dense-gas SFE ($\text{SFE}_{\text{dense}} = \text{SFR}/M_{\text{dense}}$) as a function of Σ_{stellar} . ρ_{sp} is the Spearman correlation coefficient and the p -value is for the hypothesis test as to whether they have zero correlation. The lines are local polynomial regression fits. From Jiang et al. 2020.

phologies than CO. This is consistent with HCN and HCO⁺ being faithful tracers of the dense gas responsible for the on-going star formation. Using HCN-to-CO and HCO⁺-to-CO ratios the dense-gas fractions, f_{dense} , was derived. And the ratio of CO 3–2 and CO 1–0 provides the CO-line ratio, R_{31} , an indication of the excitation condition pertaining to the total gas. It appears that f_{dense} and R_{31} both decline towards larger radii from the galaxy center. For example, at 0.5 kpc from the center, f_{dense} and R_{31} are several times lower than their values in the nucleus. The radial variation, and the large scatter of these parameters, imply distinct physical conditions in different regions of the galaxy disc.

This paper emphasized the discussion on the relationship between f_{dense} and the stellar surface density Σ_{stellar} and the relationship between $\text{SFE}_{\text{dense}}$ and Σ_{stellar} . (Figure 21), which investigate the role of existing stars on the cold gas. They both show weak increasing trends, but only

the $\text{SFE}_{\text{dense}}$ versus Σ_{stellar} relationship is statistically significant. While the f_{dense} versus Σ_{stellar} relationship is consistent with that presented in previous works using HCN 1–0 emission, it is intriguing to see an increasing trend in the $\text{SFE}_{\text{dense}}$ versus Σ_{stellar} relationship, which does not agree with other HCN 1–0 works. It remains unclear how to interpret this trend, but it is probable that this is a result of the different transitions used from other works. Considering the fact that the excitation of HCN 4–3 needs ~ 100 times higher density than that of HCN 1–0, the observations selects different components of the gas, so the existing stellar components may have a different effect on the gas traced by HCN 1–0 than by HCN 4–3. This implies that in regions with higher Σ_{stellar} the high-J dense lines of might be less sensitive to the change of the overall density and they could still trace the densest gas undergoing star formation.

These results from MALATANG show that JCMT observations can resolve

the central \sim kpc scale of nearby galaxies, allowing analysis of the variations of dense-gas parameters among different regions of galactic discs. The variation of gas properties, such as f_{dense} and $\text{SFE}_{\text{dense}}$ in different environments of individual galaxies is important for the understanding of star formation activity that regulates galaxy evolution. Other galaxies in the MALATANG sample will be studied in future papers, and deeper integration will be needed to detect the weak lines of dense gas in most disc regions. While other works have demonstrated the power of high-resolution observations using facilities like ALMA, more galaxies have to be observed in a similar manner, to reveal the true structures and properties of dense gas in the sub-structure of galaxies.

This work is published in Monthly Notices of the Royal Astronomical Society in March 2020. An open access version of the paper is available at <https://arxiv.org/abs/2003.06595>.

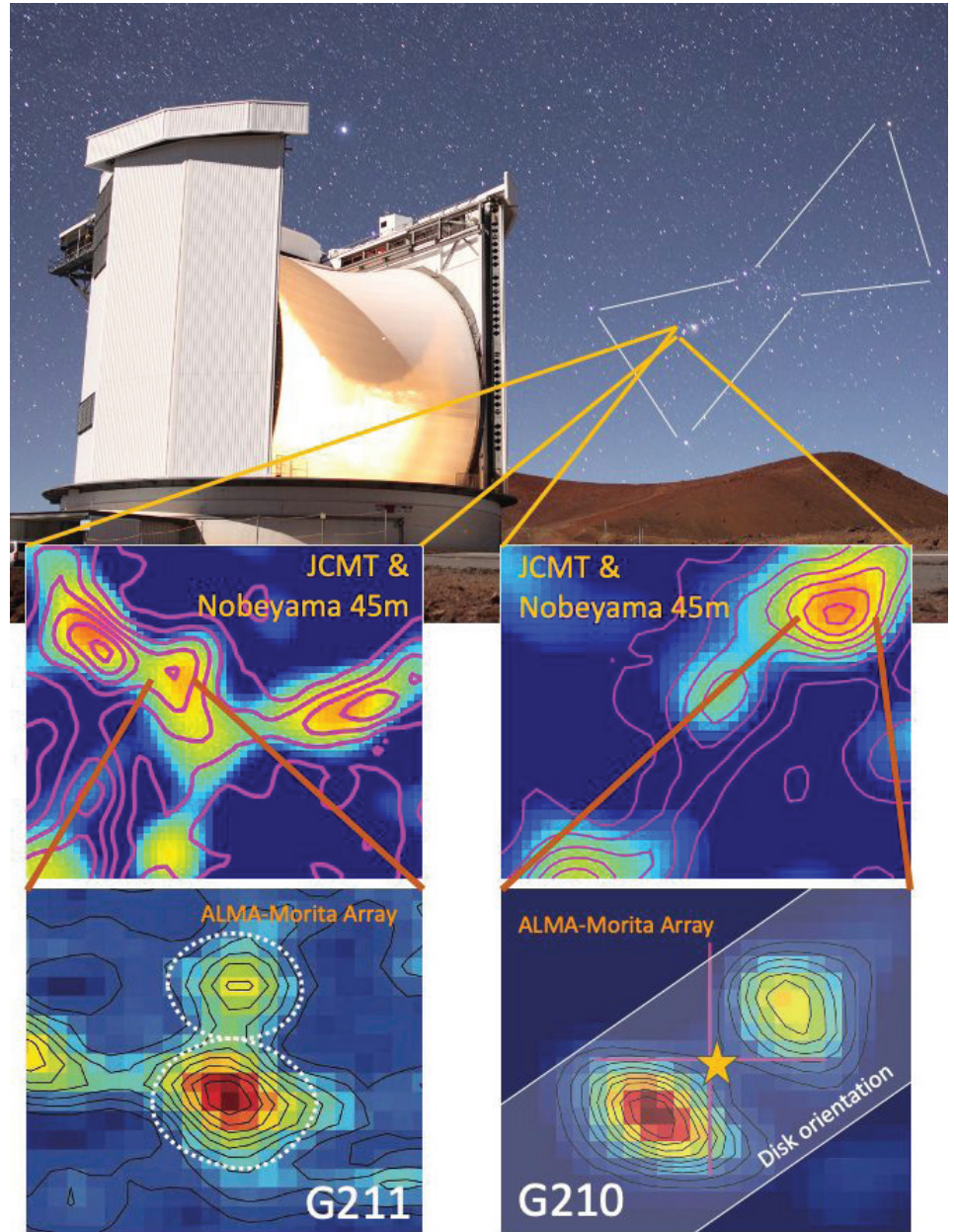
JCMT SCOPE Survey Reveals “Treasure Map” for Star Formation

Tie Liu, Shanghai Astronomical Observatory, China; Ken Tatematsu, Nobeyama Radio Observatory, Japan; and Gwanjeong Kim, Nobeyama Radio Observatory, Japan

The JCMT SCOPE Survey has provided a treasure map for astronomers studying the formation of stars. Follow-up observations using the Nobeyama 45-m radio telescope and the Morita array (ALMA/ACA) on a sample of young molecular cores that were cataloged by the JCMT survey team have revealed a multiple star system on the cusp of formation in a “starless” molecular core, a mysterious double-eye structure toward a protostar, and four new “Galactic chemical plants” (hot corinos) in the Orion constellation. These results were published in a series of three papers in the *Astrophysical Journal*.

Dr. Tie Liu, a researcher at Shanghai Astronomical Observatory, former visiting researcher at the EAO headquarters in Hilo, Hawai'i, and PI of the JCMT SCUBA-2 Continuum Observations of Pre-protostellar Evolution (SCOPE) survey, has been hunting baby stars for over a decade. The JCMT SCOPE survey targeted over 3,500 cold ($T_{\text{dust}} \sim 6\text{-}20$ K) dense cores in the Milky Way, most of which are either starless or in the earliest phase of star formation (Liu et al. 2018. *ApJS* 234:28; Eden et al. 2019. *MNRAS* 485:2895). These dense cores are “a treasure trove for astronomers investigating the very early phases of star formation,” said Dr. Tie Liu when asked about the survey, noting that “It’s great that we have powerful tools such as ALMA, but ALMA has such a small field of view, you need a telescope like JCMT to know where to look!”.

Taking advantage of the JCMT treasure map of dense cores is an international research team lead by Dr. Gwanjeong Kim, a postdoc at Nobeyama Radio Observatory (NRO), Japan, and the leading author of the paper I (Kim et al. 2020. *ApJS* 249:2) and Dr. Ken Tatematsu director of NRO, co-PI of the SCOPE



Watching the potential birth of a multiple star system

A new baby star heats up surrounding material, making its womb glow like a pair of eyes.

Figure 22. Top: Image of the JCMT with the Orion constellation highlighted (image credit: William Montgomerie). Middle: N_2H^+ maps obtained with the Nobeyama telescope; 850 micron JCMT/SCUBA-2 contours are overlaid. In the middle images, the team identified a number of dense cores. Bottom: The Morita Array reveals two different substructures within each dense core. Bottom Left: Multiple stars are seen being formed in the early starless core phase (source G211). Bottom Right: A mysterious pair of eyes appear to peer out from the disk around the newly forming star; these highlight rich chemistry occurring in the disk of this newly forming star (Results presented in paper II: Tatematsu et al. 2020. *ApJ* 895:2).

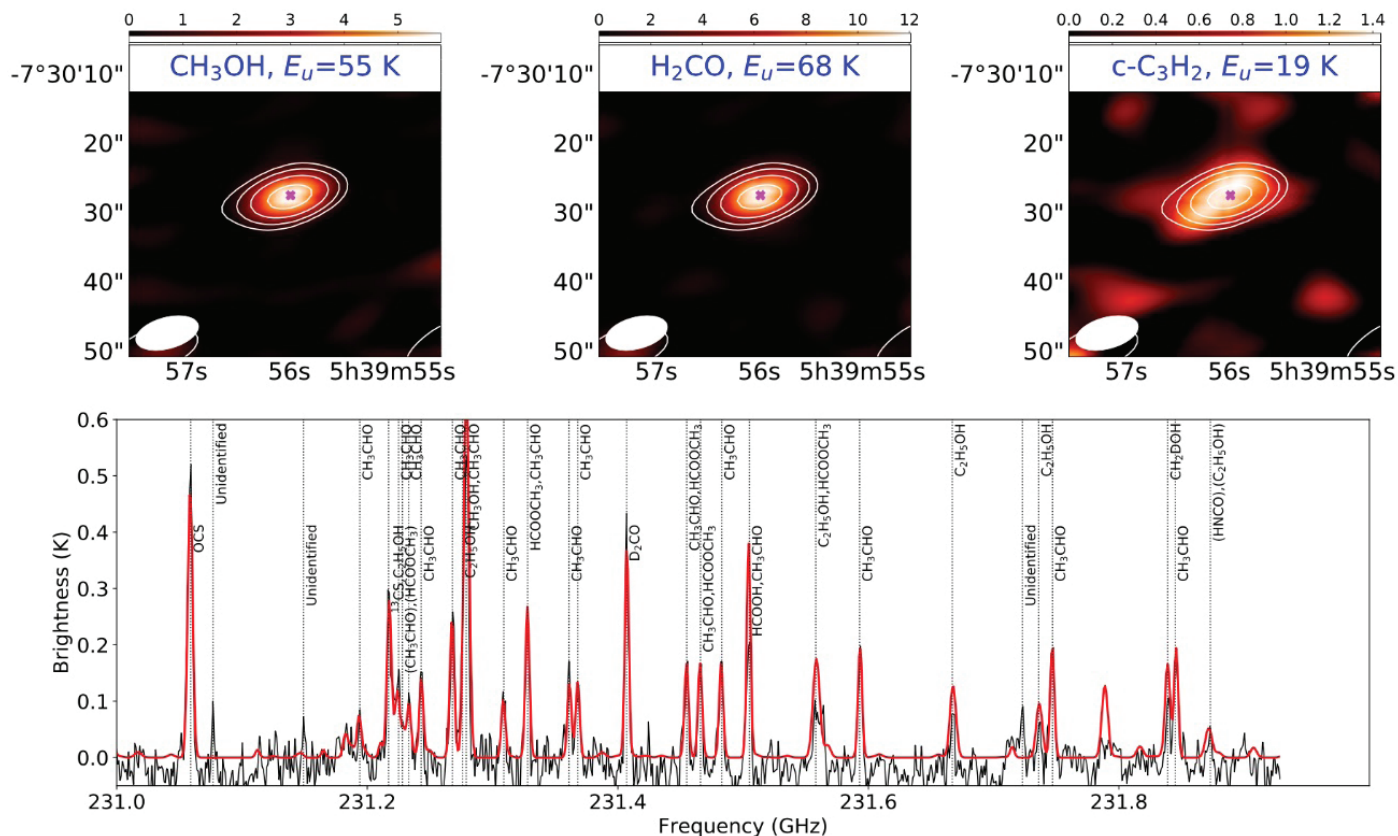


Figure 23: Upper panels: Molecular line emission maps of a hot corino. Lower panel: a spectral window of ACA observations, showing rich molecular lines. (Paper III; Hsu et al. 2020. ApJ 898:2)

survey, and leading author of paper II (Tatematsu et al. 2020. ApJ 895:2). The team have performed follow-up observations on over 200 SCOPE-identified dense cores with the NRO 45-m radio telescope. In particular, they have carefully measured the deuterium percentage in the subset of 113 cores that are found within the Orion (Kaheiheionākeiki) constellation and produced a catalog of dense cores that have a high deuterium percentage. “The dense cores that have a high deuterium percentage are places for near-future star formation. They are of great interest for investigating the onset of the birth of stars.” Said Dr. Gwanjeong Kim. Dr. Ken Tatematsu noted that “the very fast mapping capability of the SCUBA-2 instrument was essential for our research project. It was impractical to make extensive mapping observations in deuterated molecules with the Nobeyama 45-m telescope, and therefore we first surveyed candidate cold molecular cloud cores by using the SCUBA-2, which has

almost the same spatial resolution as the Nobeyama telescope. The Nobeyama 45 m telescope can observe the lowest rotational transitions of deuterated molecules around 70-80 GHz. I feel that the combination of JCMT’s SCUBA-2 and Nobeyama 45 m telescope is very powerful for star formation studies.” The team further observed the cores that had a high deuterium percentage with the Morita Array (ALMA/ACA), which is East-Asian constructed part of the world most powerful radio telescope ALMA. As a result, they obtained evidence of dense core sub-structures, unveiled a mysterious double-eye structure near a protostar, and discovered four new “Galactic chemical plants” (hot corinos):

1. Fragmentation of a starless core

A significant fraction of stars in the Galaxy are found in multiple systems. In theory, the fragmentation of starless cores gives birth to multiplicity. The fragmentation of star-

less cores, however, is hard to be captured in observations. The team, however, observed a starless core called “G211” with the Morita Array and found a clumpy structure displaying several sub-cores (see lower-left panel in Figure 22), which in turn show chemical differences. Also, the sub-cores in G211 were found to have internal motions that are almost purely thermal. The starless sub-core G211D, in particular, shows a hint of the inverse P Cygni profile, suggesting infall motion. “The detection of substructures in G211 indicates that the formation of multiple systems starts from the starless core phase”, Dr. Ken Tatematsu explained.

2. A mysterious double-eye structure near a baby star

The Morita Array observations of star forming core “G210” reveal a mysterious double-eye structure near the central protostar. It shows an interesting spatial feature of two N2D+ peaks of similar intensity and

a radial velocity profile that is symmetric with respect to the single dust continuum peak (see lower-right panel of Figure 22). "What's exciting is that in the pseudo-disk of the dense core G210, we see these two bright eyes staring back at us. This is the region around the protostar being heated and undergoing a chemical change. Usually such detail is hidden from view, but not anymore! One interpretation is that the two N₂D⁺ peaks represent an edge-on pseudo-disk." Dr. Ken Tatematsu explained.

3. New hot corinos

In 2018, the SCOPE team initiated a new survey project at ALMA (ALMASOP; PI: Dr. Tie Liu), observing 72 SCOPE dense cores in the Orion constellation. The ALMASOP team has recently published first results, reporting the detection of four new hot corinos with the Morita Array (see Figure 23). "Hot corinos are dense cores characterized by

the presence of abundant saturated complex organic molecules (COMs) within a warm (~100 K) and compact (< 100 au) region around the central protostar. They are of great interest for studying the origin of pre-biotic molecules and life." explained by Dr. Sheng-Yuan Liu, a researcher at ASIAA and co-PI of the SCOPE survey. "With the Morita Array, we have identified four new hot corinos, but we have identified more from the ALMA 12-m array data of ALMASOP. The number of known hot corinos will be doubled from our research." added Shih-Ying Hsu, a PhD student at National Taiwan University and the leading author of paper III (Hsu et al. 2020. ApJ 898:2).

These results offer important clues to understand how stars begin to form. Commenting on the future of this work, Dr. Tie Liu said "We will do more systematic studies of these SCOPE dense cores with high resolution interferometric observations

(e.g. ALMA); who knows what other treasures will be found!"

This work has been published in the following three papers:

Paper I: Kim et al. "Molecular Cloud Cores with High Deuterium Fraction: Nobeyama Single-Pointing Survey" (<https://iopscience.iop.org/article/10.3847/1538-4365/aba746>)

Paper II: Tatematsu et al. "ALMAACA and Nobeyama Observations of Two Orion Cores in Deuterated Molecular Lines" (<https://iopscience.iop.org/article/10.3847/1538-4357/ab8d3e>)

Paper III: Hsu et al. "ALMA Survey of Orion Planck Galactic Cold Clumps (ALMASOP): I. Detection of New Hot Corinos with ACA" (<https://iopscience.iop.org/article/10.3847/1538-4357/ab9f3a>)

A Decade in the Making: Celebrating a Year of Successful Remote Observing

Harriet Parsons, Head of Operations, EAO/JCMT

On November 1st 2019 the JCMT observatory switched from summit observing on Maunakea to remote operations from the JCMT/EAO sea-level base facility in Hilo. For some this has felt like the end of an era, and for others it has lifted the burden of providing observers. The timing of the switch has been noted by many to be fortuitous with regards to the current COVID-19 pandemic. Remote Observing has enabled the observatory to adapt to social distancing policies and restricted staff access to the facility, all the time maintaining the production of high quality data in a safe and efficient manner.

This successful switch to Remote Observing came after a decade-long effort by JCMT staff. Under the operations of the Joint Astronomy Cen-



Figure 24: JCMT Telescope Operator Patrice Smith undertaking JCMT observations from the JCMT Remote Control Room (JROC) at the EAO/JCMT sea-level base facility in Hilo.

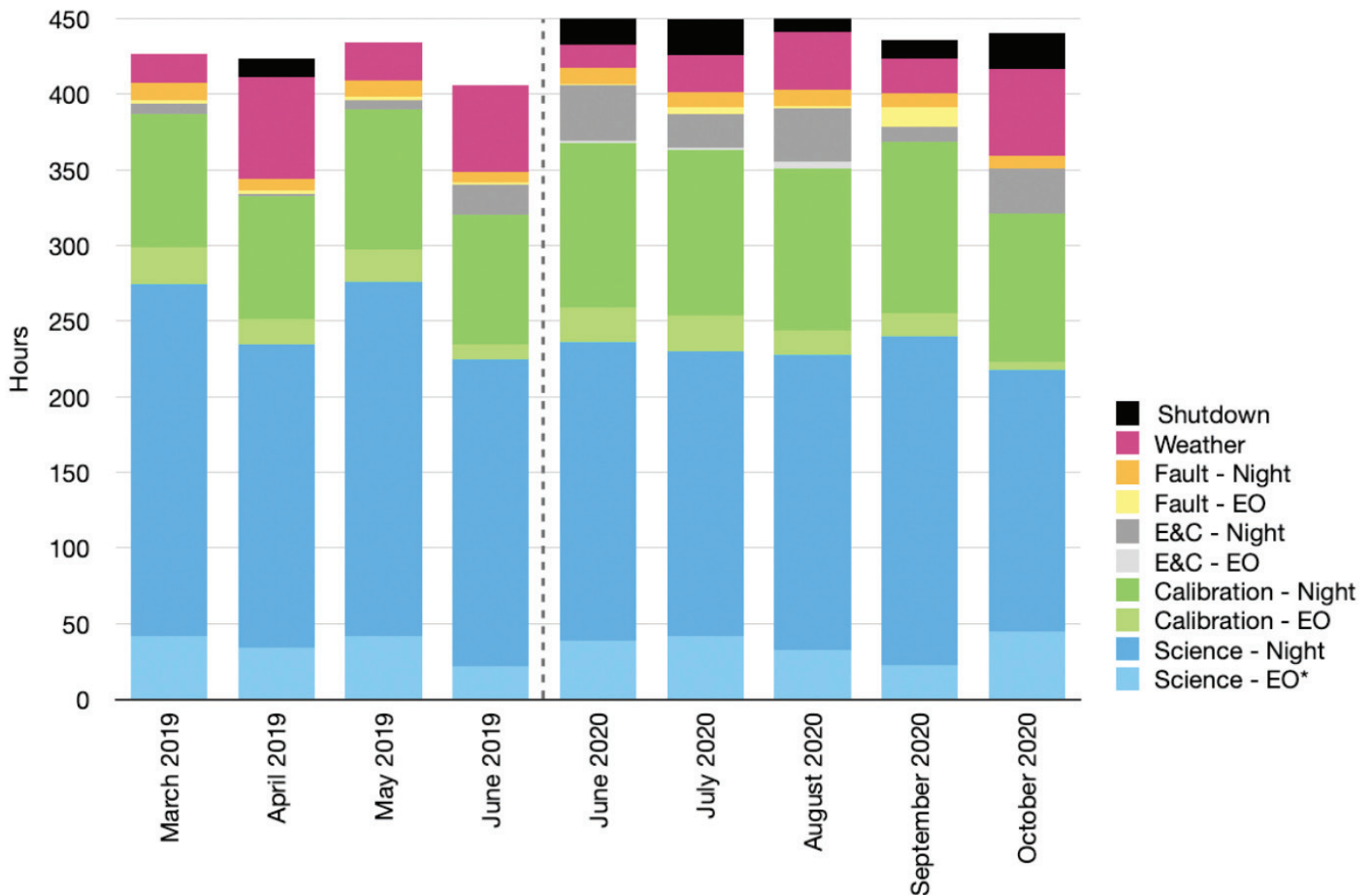


Figure 25: Observatory hours broken down by category. Science, Calibration, Engineering and Commissioning(E&C), Fault, Weather (time when observatory was closed due to weather), and Shutdown (time when observatory was closed). The months displayed are 1) four months (March - June 2019) prior to shutdown due to the restricted access on Maunakea when the JCMT was operated from the summit. 2) the five months after the return to operations (June - October 2020) from global pandemic shutdown when the JCMT was operated remotely. The time gap and switch to Remote Operations are indicated by the dashed vertical line.

tre¹ UKIRT successfully switched to remote operations in December 2010. The lessons learned from this switch enabled staff to benefit from existing shared software and policies, and other insights from this process ten years prior. Implementing the lessons learned from the 2010 UKIRT switch came in 2013/2014 at the JCMT - when funding pressure led to a push to gain additional hours of operations - leading to what is now referred to as Extended Operations (EO) - operation of the telescope beyond the typical night shift (typically from 7am to 10am).

The first step required the control

¹ Historically the Joint Astronomy Centre (JAC) operated the United Kingdom Infra-Red Telescope (UKIRT) until October 31st 2014 and the James Clerk Maxwell Telescope (JCMT) until March 1st 2015.

of the roof and door closure and drive systems remotely. In addition, the implementation of a deadman handshake for power interruptions and safety. Further, we required the installation of six interior and exterior cameras, including an infrared camera - to ensure the safety of both people, equipment and enabling telescope operators to check for fog. Finally setting up the JCMT Remote Observing Control Room for the operator at the sea-level base facility - known as JROC. After extensive work on the facility and testing Extended Observing officially began in January 2014 (for further details see JCMT Newsletter article #35).

Extended Observing in 2014 demonstrated that partial remote operation of the JCMT from Hilo was

possible. That was the first major soft test for the system. The second soft test along the road to remote observing came two years later in 2016. Effort was made to enable a key staff member to continue working through her pregnancy operating the telescope (not advisable at high altitude). This meant that the JCMT was essentially operating remotely for 5 nights out of 15. Full summit nighttime operations at the JCMT resumed later that year.

The final stage of the shift to remote operations came in 2019. Staff had confidence that the switch to remote observing could be made in a safe and efficient manner. This confidence came from past examples of remote operations of the facility. It also came from confidence in the instrumentation and software used

to maintain the high level of data quality our users have come to expect and rely on (e.g. ORAC-DR, OMP, JCMT Science Archive, hosted at CADC and internal EAO/JCMT staff accessible archive tracking pages). Final effort by staff involved:

- Shifting final systems onto remote power switches/control
- Electrical and pneumatic roof and door upgrades
- Review of safety and weather policies
- Expanding remote monitoring/control of instrument systems

Now 12 months on from the switch to remote operations it is possible to assess how well remote observing has been progressing at the observatory. A comparison of the pre- and post-remote operational metrics, including the fault rate and productive time on-sky, provides a measure of the success of the JCMT under remote operations. For this comparison the observatory performance pre-remote operations (between March² and June 2019³), is the operational performance, post-remote operations (between June and October 2020).

A breakdown in the hours spent during night time and EO by month is provided in Figure 25. A summary table, looking at per-night-averages, is provided in Table 1. Looking at the total number of productive time (as provided in Table 1), on average the observatory is now obtaining more productive hours since the switch to remote operations (despite the slight increase in fault rate). The productive hours on the telescope have increased by approximately one hour per night which is with the time taken for a TSS and observer to take a round-trip between Hale Pohaku (the base accommodation

2 Since March 2019 the JCMT time accounting software tracks the number of hours spent on sky on a per-shift basis- Night-time, Daytime and EO - previously EO hours were not tracked to the same level of detail.

3 The Summer 2019 operational hiatus resulting from restricted access to Maunakea began July 2019 and an extremely wet observing season Autumn/Winter 2019 and second operational hiatus (March - May 2020) due to COVID-19

	Average per night (2019) †		Average per night (2020) ‡	
	Night Time	EO	Night Time	EO
Science (hrs)	8.2	1.3	7.4	1.1
Calibration (hrs)	3.3	0.7	4.1	0.6
E&C (hrs) §	0.3	0.0	1.0	0.1
Productive Time (hrs)	11.7	2.2	12.5	5
Fault Rate (%)	3.0	4.8	3.1	8.7
Overall fault rate (%)	2.9		3.4	

Figure 26: Summary table of JCMT performance before and after the switch to Remote Observing, for a four month window in 2019 and a five month window in 2020. Hours per night account for closures due to observatory shutdown and weather. Productive time includes hours spent on Science, Calibration and Commissioning. †March-June 2019: after an update to operational time accounting and prior to restricted Maunakea access. ‡June-September 2020: after the COVID-19 JCMT operational hiatus. §E&C: Engineering and Commissioning.

facility for observatory staff working on Maunakea) and the JCMT. The other notable change in Table 1 is an increase in calibration and E&C time. This is the result of commissioning the new heterodyne instrument Nāmakanauī, which saw first light on the telescope in October 2019. The fault rate has remained consistent at or below 3% following the switch to remote operations and well below the Observatory target of less than 5%, without a single instance of the TSS requiring access to the facility to resolve a fault in the past 12 months.

JCMT staff are proud of this efficient and smooth switch to remote observing. Our highly trained telescope operators, fantastic instrumentation and a software suite ensures the JCMT continues to obtain high data quality without the need of a visiting astronomer at the telescope.

With that being said the observatory recognizes the value of facility visits by astronomers - particularly new users. Anecdotally it has been noted that astronomers who visited JCMT in the past have become more engaged users, benefiting from direct staff interaction, improving their understanding data quality, instrument capabilities and has allowed them to write better proposals. Ultimately these astronomers can see a shorter turnaround between data collection and publication. With this

in mind although the JCMT is now Remote Observing we will continue to seek meaningful ways to engage and connect with our user community. In early December JCMT staff held a Virtual Workshop for astronomers from Malaysia, Thailand, Indonesia, and Vietnam. The observatory hopes to once again resume the JCMT Users Meeting in a post-pandemic world, and is excited to launch a community engagement program to support early career astronomers in the future. Under this program, early career astronomers will be invited to visit the Hilo sea-level observatory facility for a period of a few weeks, given the opportunity to visit the telescope and to collaborate with science staff. Finally although observers will no longer be required at the observatory to assist with data collection, PIs and COIs of programs - are welcome to “eavesdrop” on operations by joining a remote connection directly to JROC in Hilo via a zoom link provided in an automated email that is generated any time a PI’s program starts obtaining data at the observatory on a given night.

This work has been presented at the SPIE 2020 Astronomical Telescopes + Instrumentation Digital Forum under “Implementing remote observing at the JCMT” and can be found at: <https://arxiv.org/abs/2012.10568>.

‘Ū‘ū Commissioning Update

Dan Bintley, Instrument Specialist, EAO/JCMT

JCMT staff have been working hard to finish the on-sky commissioning for ‘Ū‘ū, the 230GHz (Band 6) receiver of Nāmakanui, which is the duplicate of the receiver deployed at GLT, and constructed and on loan from the ASIAA GLT team. ‘Ū‘ū is currently being used nightly for shared risk science and will be released to the full user community very soon.

2020 has been such an enormously difficult year for everybody both in Hawai‘i and around the world. To imagine that we could commission a new instrument, while maintaining normal telescope operations, this is a tremendous achievement.

We would especially like to highlight the contribution provided by ASIAA and by the JCMT user community, including the JINGLE and NESS large program teams and PIs who have been participating in shared risk science. Without this support we would not have such rapid progress. You have helped us to chase down and fix some of the many software and instrumental bugs, that could have impacted data quality while demonstrating the excellent performance of the instrument.

The “First light” after installing and aligning the cabin optics for ‘Ū‘ū came in October 2019 quickly followed by the first VLBI fringes.

In addition to installing Nāmakanui, we have also installed a complete stand-alone VLBI backend for JCMT. The first EHT VLBI test and first fringes with the SMA was in December 2019. This demonstrated the phase stability of the receiver frontend. While later (February 2020) East Asian VLBI tests with the GLT, which also produced fringes, came from data recorded to disk and later correlated in Shanghai.

We started 2020 by replacing a mixer block. Each polarization has two mixers. One of the P0 mixers was found to be susceptible to thermal cycling. A replacement mixer block

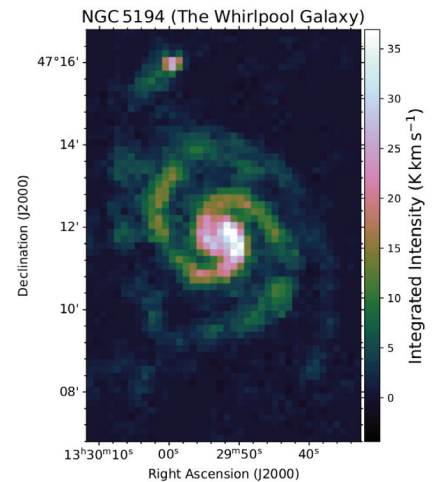
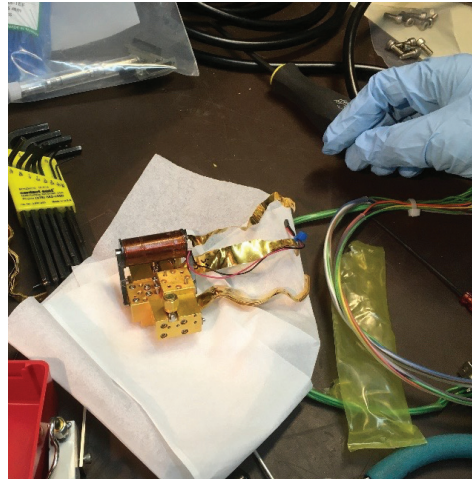


Figure 27: Left: Installing new Band 6 mixer block. Right: CO (2-1) Integrated intensity map of M51 also known as the Whirlpool Galaxy, NGC5194.

was sourced from NRAO and delivered to Hawai‘i in the last week of 2019. Our colleague Johnson Han from ASIAA flew into Hawai‘i to help dismantle the Band 6 cold cartridge and install the new mixer block. We faced not only the coming COVID storm, but also Arctic conditions at the summit as we installed and tested the new mixers. The new P0 mixers are fully functional.

Nāmakanui was cold and operational just before we suspended summit operations, in response to the virus. We kept our new instrument cold and ready to go, while staff started working from home. Soon all Hawaii non-essential businesses were also shutdown.

Remote JCMT operations started again in May and with that on-sky commissioning could begin in earnest. It has been apparent from the start that the on-sky performance is excellent, and that users will really benefit from the performance gains over RxA and RxA3m. However, it has not been totally smooth sailing and a number of bugs had to be found and fixed, mostly introduced due to the differences of a dual polarisation 2SB receiver compared to the previous single polarisation dual sideband receivers. The new receiver design provides much improved sensitivity and increased science capability.

There remain a few hardware issues to solve, including baseline features due to antenna motion in position switched observations and LO fringing (a periodic change of LO power in frequency space). The LO fringing can be worked around, by careful choice of tuning frequency and positioning of the lower and upper sidebands. We provide the tools for our users to make this choice easily when creating an MSB.

In conclusion, 2020 has been the most difficult and challenging year and yet at the end of it we have a new instrument for JCMT, that is already producing excellent science and will only get better. The JCMT commissioning team has a full document ready to share with the community, that will provide all of the relevant commissioning results, receiver characteristics and user examples to help make the best scientific use of our new eye on the universe.

And this is just the beginning. Before the year end, we will have first light with ‘Āweoweo the 345GHz (Band 7) receiver. 2021 promises so much more.

This work has been presented at the SPIE 2020 and can be found at: <https://arxiv.org/abs/2012.07349>.

JCMT Ice and Snow Melting Program

Craig Walther, Chief Engineer, EAO/JCMT

Anyone who has been to the summit of Maunkea during sunny daytime hours realizes that the Sun's rays are very intense at that altitude. It has been known for years that the Sun is very helpful when clearing ice and snow from the telescope. In fact, it is sometimes almost unbelievable how helpful it is.

Occasionally parts of the telescope will be covered in a layer of ice. If the telescope is rotated such that this layer is in the Sun, water begins to form between the ice and the telescope structure almost immediately. This even happens when the temperatures are well below zero centigrade. The ice is translucent to most of the Sun's energy and the telescope structure absorbs most of that energy. This heats up the surface of the structure, which quickly melts the ice. Soon after the water forms under the ice, the ice layer will begin to slip off the telescope; this process can be accelerated by slightly tapping the ice with a shovel. The snow that accumulates on the telescope often is accompanied by an underlying ice layer. This is due to the structure being slightly above zero degrees when it starts to snow, or rain turning into snow in the evening as the environment cools down. This ice layer makes it very difficult to shovel the snow. If the telescope is rotated into the Sun and a small portion of the snow is cleared and the ice chopped away from the structure, the Sun immediately begins to warm the structure weakening the ice-structure interface and allowing a shovel to "pop" the ice off the structure.

The snow crew has positioned the areas of the telescope, where they are working, into the Sun for years. This was usually done by one person driving the telescope while talking to another person at the work area, via a walkie-talkie. This is a tedious procedure since it is very difficult to judge just how many degrees to move the telescope when you

are standing on top of it and looking at the sun. Also, the snow crew would position the telescope and then head up to the roof to clear snow. Soon the motion of the Sun would make the telescope's position less effective for snow clearing, as parts of the roof move into shadows. Whenever there is a slight angle between the back end of the telescope and the Sun, one of the sides of the gantry is put into shadow. When this happens on a cold day, that side ices up quickly and is very difficult to clear.

There are three locations on the telescope, where snow accumulates, that must be cleared to safely open the roof and doors: the roof itself and the tracks the left and right doors move on while opening. Also the gantry itself must be cleared of ice before opening the roof. Therefore, there are seven primary locations on the telescope where it is important to direct the Sun's rays: right

door track, left door track, roof directly, left outside gantry, right outside gantry, left inside gantry and right inside gantry.

A program was written (called melt-Snow) that determines the local time and then calculates the current azimuth of the Sun at JCMT. Using the walkie-talkie method, the angle to place each of the seven locations directly into the Sun was determined. The program has these angles stored in it. When the program is started, it determines the number of minutes between the present and 5:00PM and divides that number by seven. It then commands the telescope (using the nighttime telescope control system) to the first position. That position is determined by subtracting the measured angle from the calculated current azimuth of the Sun. The telescope is then commanded to move every 30 seconds to follow the Sun. This continues until 1/7 of the time to 5:00pm is



Figure 29: EAO Staff clear the snow and ice from the roof in February 2020.

exhausted and then the telescope is moved to the next position. This way the telescope sits in each of the seven positions equally during the entire day.

The same program can be run in a different mode where it moves to one specified position and then follows the sun in that position until told to move to another position. This mode is meant for the snow crew who usually want the position they are about to clear, or are clearing, to stay directly in the Sun until they are finished.

One problem with this method of melting snow and ice are the limit switches on the gantry that tell when the roof is approaching the end of the gallery and stop the roof's mo-

tion. These switches are inside of protective covers and can ice up themselves. These switches can be damaged if the roof hits them while they are covered in ice. The protective covers keep ice and snow off the switches, but they also keep the sun off the switches, making it hard to melt their ice with the Sun. Plexiglas switch covers could possibly help this situation. After measuring the seven positions it was noticed that the outside right gantry position and the inside left gantry position are nearly identical. This is the same of the outside left gantry and inside right gantry. It is likely that two of these positions could be eliminated.

Before JCMT moved to remote observing the TSS was required to drive to the summit early in the morning

after snowy weather. The TSS would inspect the telescope and then contact the snow crew leader with that information. This is no longer possible, as the TSS is running the telescope from Hilo. Therefore, the TSSs now check the cameras at the summit, if it appears there has been snow or ice accumulation, the TSS starts the meltSnow program and contacts the snow crew leader. The Office of Maunakea Management has been asked to approve four new cameras for JCMT two on each of the penthouses to inspect the roof closely and one on each of the door ends, so the tracks can be inspected. Until these cameras are installed, the snow crew will go to the summit if there is any indication that snow or ice removal is required.

Maunakea Wonders Teacher Workshop

Callie Matulonis, Telescope System and Outreach Program Specialist, EAO/JCMT

The East Asian Observatory, in collaboration with the University of Hawai'i at Hilo (UHH) Department of Education, piloted the Maunakea Wonders Teacher Workshop (MWTW) in June 2017. With a focus on connecting local newly qualified teachers to the observatory and educational resources, we have been able to develop and successfully host five workshops with an overwhelmingly positive response resulting in the MWTW becoming the flagship Education and Public Outreach event led by EAO.

The primary goal of the MWTW is to highlight the Maunakea Observatories as an accessible resource for new teachers in the State of Hawai'i at the start of their careers. Students in the Masters in Teaching Program at UHH are provided the workshop free of charge and it is offered as part of their curriculum with teachers gaining course credit for attendance.

When analyzing the outreach needs of our community in 2017, we realized that there was an opportunity to equip teachers in train-

ing with additional connections and resources they could access in order to feel supported when sharing information on science, astronomy and Maunakea with their students.

Since its inception, the Maunakea Wonders Teacher Workshop has hosted 80 participants. A pre-survey

is conducted prior to each workshop to analyze the participants grade and subject levels, pre-conceptions and knowledge, as well as what they hope to learn from the program.

Each workshop has been designed and modified based on feedback

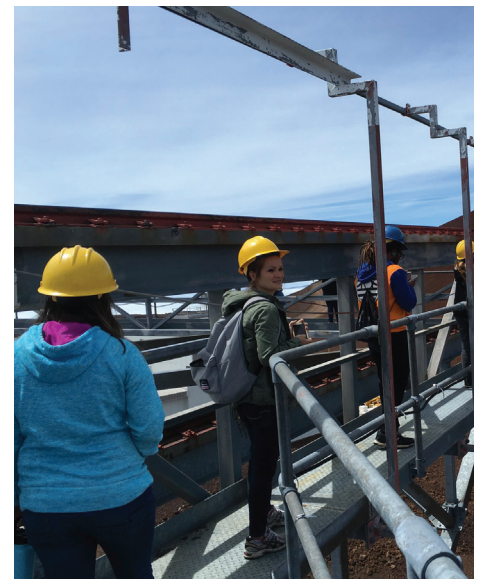


Figure 30: Left: A MWTW participant showing the constellation mobile she created to demonstrate stellar distances in an example classroom hands-on activity. Right: MWTW participants take in the view along the catwalk around the roof at the JCMT in 2018.



Figure 31: 2019 Maunakea Wonders Teacher Workshop participants were treated to a private planetarium show at the 'Imiloa Astronomy Center.

from prior attendees. For example, the first workshop was held at the EAO base facility during summer break. Many of the comments stated that more of their classmates would have attended if the workshop was held during the school year or with an option to earn credits. EAO and UHH worked together to arrange for subsequent workshops to be held in their UHH classrooms during the semester, and to offer the summit tour portion of the workshop as a Professional Development credit.

The format of each workshop consists of classroom activities and a summit tour. For the classroom activities, the MWTW coordinator arranges for a variety of presentations, the majority of which are presented by EAO staff. The presentations usually take place over the course of two days spending two hours each day in their classroom. Each presentation is on average 30 minutes long with the objective to be highly engaging while demonstrating hands-on, meaningful activities that could be implemented in their own classrooms. We have found that offering the summit tour portion sandwiched in between the two classroom visits allows for there to be some excitement building and information delivered prior to the tour followed by time for reflection and questions afterwards.

The classroom curriculum is adjusted based on presenter availability and expertise, but key elements include a cultural presentation, an overview of the resources on Maunakea (astronomical, cultural, geographical, environmental, and the stewardship efforts), a basic introduction to astronomy and light, a portable starlab planetarium presentation and training, and a career panel highlighting the variety of observatory jobs.

Transportation for the summit tour portion of the workshop is provided by EAO in the form of rented 4WD 15-passenger vans. To acclimatize, we stop at the Hale Pohaku mid-level facility for lunch, a safety briefing, and a cultural presentation before ascending the summit. After which we continue up the mountain where we visit two telescopes. JCMT is always an included telescope on the tour, and we have also taken the participants into UKIRT and the CFHT.

The MWTW ends with a final survey to assess each portion of the workshop and each attendee is provided a goodie bag with various stickers, mugs, magnets, and other handouts. All presentations and electronic resources are provided containing each presentation, as well as step-by-step instructions for

hands-on activities in the classroom, and a list of contacts at the observatories that they may reach out to with questions or requests.

Keeping an open dialogue with past attendees is important and more effort has been made to reach out a few times throughout the year to remind them that we are here if they need presenters, science fair judges, ideas for classroom activities and to provide them with information on events we are engaged in that they may want to attend or pass along to their students.

The most recent workshop was held virtually at the end of October 2020 in light of the COVID-19 pandemic. The workshop continues to be a priority amongst our outreach efforts as we value the connection formed with the local educators in our community, and want to support them in any way possible, especially during the current challenges they may be facing.

Our partnership with the UHH Department of Education and our past MWTW participants continues to evolve and strengthen as we strive to improve the program with each occurrence. We look forward to growing these relationships and the opportunities that may develop from this community engagement.

A Hui Hou

Jim Hoge, Telescope System Specialist (Retired), EAO/JCMT

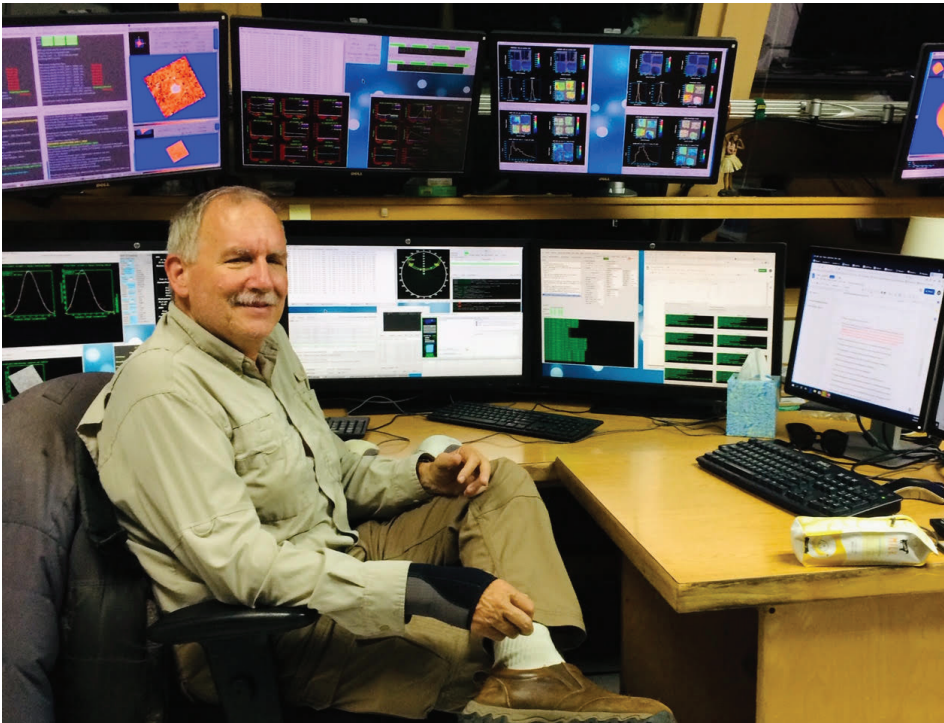


Figure 32: Jim Hoge at the summit Telescope System Specialist station in the control room at the James Clerk Maxwell Telescope.

Working as a Telescope System Specialist at JCMT was the perfect capstone to 44 years of adventure (Navy + JCMT). After traveling under the polar ice cap, operating submarines in hundred foot seas in the North Atlantic and voyaging in every ocean except the Indian Ocean and Antarctic; the 19.5 years I spent operating JCMT at the summit of Mauna Kea was my most exciting, fulfilling and challenging job. From my first shift to my final night observing, I learned from the Astronomers and students with whom I had the pleasure to observe. My success can be attributed to scientists sharing their passion and their enthusiasm over more than 2300 nights on Maunakea. Our Astronomy community made me feel needed and appreciated through some very challenging times. I am proud of what we accomplished and hold dear the many friends I have found around the world.

2020 - The EAO 'Ohana's Year in Review

Callie Matulonis, Telescope System and Outreach Program Specialist, EAO/JCMT

We have seen some big changes at EAO since our last newsletter. Our beloved Telescope System Specialist, Jim Hoge, retired after nearly 20 years at JCMT. Having worked closely with Jim, I can say with only a hint of hyperbole that I didn't think we could survive without him. Jim's history at JCMT is a rich one - filled with stories of obtaining hard to get data that resulted in monumental discoveries, finding solutions only someone with his unique background as a Naval Commander could imagine. Jim was a firm favorite among astronomers who visited the telescope from fresh-faced grad students to professors alike. He truly was deserving of the award for "Most Dedicated Employee."

As a TSS, he called to check in around 1am every single night to

see how operations were going. He knew how to resolve faults that were far beyond the expectations for the TSS position. If you needed someone to go up to the summit at any time of day or night for any reason, he would not hesitate to drop everything to be there. I remember casually mentioning to him over the phone one night that the coffee maker had broken at the summit. By the next night, I had found out that he went to the store, purchased a new one, and drove it up to the summit himself to make sure my observer and I had coffee.

I could go on, but I'll finish by saying that those are some big shoes to fill and I'm sorry that staff entering the post-Jim era will only hear the stories that light up everyone who speaks of him. I, for one, miss my frequent

interactions with him tremendously and sincerely hope he is enjoying his well-deserved retirement.

A hui hou as well to outreach extraordinaire Mimi Fuchs who left the Telescope System Specialist position in September to accept a graduate fellowship in Systems Engineering at Drexel University in Philadelphia, PA. She will be staying on island and completing her masters degree remotely.

Welcoming into our awesome EAO 'ohana we have Patrice Smith. Before joining our Extended Operations team in November 2019, University of Hawai'i at Hilo astronomy graduate, Patrice, was working as a research assistant for Dr. Heather Kaluna and as a planetarium operator at the 'Imiloa Astronomy Cen-

ter. After nearly a year of operating the JCMT for extended operations, Patrice was recently promoted to a full-time JCMT Telescope System Specialist. She is thrilled to be operating at the JCMT, and recently enjoyed assisting in the Comet NEO-WISE observations. Her favorite thing about her job is seeing how all aspects of the observatory work and come together.

Big Island born and raised, Mailani Neal, completed her 3rd internship at JCMT with the instrument science group this summer. Her focus this summer was in assisting various tasks associated with the commissioning of the 'Ū'Ū receiver in the Nāmakanui instrument. Some of her tasks included collecting receiver temperature measurements, data reduction of standard calibration sources observed by 'Ū'Ū and comparing those observations with the RxA observations. She also assisted in identifying calibration sources for the 'Āweoweo receiver. She is cur-

rently working on her master's degree in physics with a specialization in astronomical instrumentation at the New Mexico Institute of Mining and Technology.

Before coming to Hilo, Pablo Torne, our EAO Visiting Scientist, was a post-doctoral researcher at the Instituto de Radioastronomia Milimetrica in Spain, commonly known as IRAM. During his time at EAO, he continued to help with the instrumentation at IRAM and at JCMT as well. He made sure certain parts of the telescope worked as expected and delivered nice data to our users. At the same time, he also used the telescopes for astronomical research focusing on a very special type of star called magnetars - the strongest magnets known in the Universe. He returned to Spain in October 2020.

Xue-Jian Jiang joined us as an EAO Fellow after having previously worked at the Purple Mountain Observatory in Nanjing, China. He is

currently working to better understand star formation processes in the interstellar medium of the Milky Way and other galaxies by conducting observations with astronomical millimeter and sub-millimeter facilities like the JCMT. His goal is to address questions concerning the relationship between different phases of gas, specifically high-density gas, and star formation.

Haley Reese joined our Computer Systems Group in November 2019 as an Information Technician. Haley is proud of the CSG team in how they have adapted their communication style over the last few months and is happy they have been able to remotely work together as a team on some of the tasks that have been prioritized recently.

Thanks for being a part of our 'oha-na. Take good care of yourself. From our family to yours. Aloha!



Figure 33: Top Row Left to Right: Jim Hoge, Mailani Neal, Xue-Jian Jiang, and Patrice Smith.

Bottom Row Left to Right: Mimi Fuchs, Haley Reese, and Pablo Torne.

